CWP-820
May 2014



3D radio reflection imaging of asteroid interiors

Detchai Ittharat

- Master of Science Thesis -
Geophysics

Defended on May 1, 2014

Advisor:	Prof. Paul Sava
Committee Members:	Prof. Jeff Andrews-Hanna
	Robert Grimm, PhD
	Prof. Roel Snieder

Center for Wave Phenomena
Colorado School of Mines
Golden, Colorado 80401
303.384.2178
http://cwp.mines.edu

3D RADIO REFLECTION IMAGING OF ASTEROID INTERIORS

by

Detchai Ittharat

ABSTRACT

Imaging the interior structure of comets and asteroids in 3D holds the key for understanding early Solar System and planetary processes, aids mitigation of collisional hazards, and enables future space investigation. 3D wavefield extrapolation of time-domain finite differences, which is referred to as reverse-time migration (RTM), is a tool to provide high-quality images of the complex 3D-internal structure of the target. Instead of a type of acquisition that separately deploys one orbiting and one landing satellite, I discuss dual orbiter systems, where transmitter and receiver satellites orbit around the asteroid target at different speeds. The dual orbiter acquisition can provide multi-offset data that improve the image quality by illuminating the target from different directions and by attenuating coherent noise caused by wavefield multi-pathing. Shot-record imaging requires dense and evenly distributed receiver coordinates to fully image the interior structure at every source-location.

I illustrate a 3D imaging method on a complex asteroid model based on the asteroid 433 Eros using realistic data generated from different acquisition designs for the dual orbiter system. In realistic 3D acquisition, the distribution and number of receivers are limited by the acquisition time, revolving speed and direction of both the transmitter and receiver satellites, and the rotation of the asteroid. The migrated image quality depends on different acquisition parameters (i.e., source frequency bandwidth, acquisition time, the spinning rate of the asteroid) and the intrinsic asteroid medium parameters (i.e., the asteroid attenuation factor and an accurate velocity model).

A critical element in reconstructing the interior of an asteroid is to have different acquisition designs, where the transmitter and receivers revolve quasi-continuously in different inclinational and latitudinal directions and offer evenly distributed receiver coordinates in the shot-record domain. Among different acquisition designs, the simplest orbit (where the transmitter satellite is fixed in the longitudinal plane and the receiver plane gradually shifts

in the latitudinal direction around the asteroid target) offers the best data coverage and requires the least energy to shift the satellite. To obtain reasonable coverage for successfully imaging the asteroid interior, the selected acquisition takes up to eight months. However, this mission is attainable because the propulsion requirements are small due to the slow ($<$ 10 cm/s) orbital velocities around a kilometer-sized asteroid.

TABLE OF CONTENTS

ABSTRACT iii

LIST OF FIGURES vi

LIST OF TABLES x

ACKNOWLEDGMENTS xi

CHAPTER 1 INTRODUCTION 1

CHAPTER 2 3D ELECTROMAGNETIC WAVE EQUATION MODELING 4

2.1 Electromagnetic wave equation and finite difference scheme 4

2.2 3D model building 7

2.3 Wavefield and data 11

CHAPTER 3 3D IMAGING 19

3.1 Wavefield reconstruction and imaging condition 19

3.2 Migrated image quality using varied receiver coverage 21

3.3 Migrated image quality using different velocity models 23

CHAPTER 4 3D ACQUISITION DESIGN 28

4.1 Navigation and data collection design 28

4.2 Realistic acquisition design 30

4.3 Alternative acquisition designs 34

CHAPTER 5 DISCUSSION AND CONCLUSION 56

REFERENCES CITED 59

LIST OF FIGURES

Figure 2.1 3D synthetic velocity model based on asteroid Eros 433. The model consists of spherical blocks that represent rock fractures (darker color) and the matrix around the rock that represents regolith (softer color). The upper right figure shows 3D slices through the asteroid model in 3D view. 10

Figure 2.2 Shot locations are evenly distributed on the source geodesic dome (1.9 km radius). The receiver geodesic dome is dense and located at a 0.55 km radius. Each shot location has its own shot-record receiver coordinates within a small region corresponding to 60 degrees aperture relative to shots (a) 0, (b) 64, (c) 128, (d) 192 14

Figure 2.3 Using the analytic Green's function, I shift the source wavelet from the transmitter (located at 1.9 km) to the closer orbits (0.55 km radius) around the asteroid target. The data in panels (a)-(d) correspond to the source and receiver locations shown in the panels of Figure 2.2. 15

Figure 2.4 Wave propagation using a time-domain electromagnetic finite difference scheme. The wavefield snapshots correspond to the geometry depicted in panel (a) of Figure 2.2 with increments of 1000ns 16

Figure 2.5 Wavefield snapshots (zoomed in view of Figure 2.4) at panel (a) of Figure 2.2 for time (a) 1000 ns and (b) 1250 ns. These snapshots illustrate the complex and attenuative wavefields when the wave propagates into the asteroid model. 17

Figure 2.6 Reflected data (collected on receiver geodesic dome) located at 0.55 km radius (near array). In these figures, I show the attenuation effect using different conductivity levels inside the asteroid model. Observed data (without attenuation) correspond to source and receiver coordinates from panels (a)-(d) in Figure 2.2 are shown in (a)-(d), respectively. Observed data (with medium attenuation) are shown in (e)-(h) with respect to source and receiver locations above. 18

Figure 3.1 Imaging experiment using 10 MHz frequency, true velocity mode, medium attenuation, dense and evenly distributed receiver coverage: (a) migrated images with complete acquisition ($N_e = 320$ shots), (b) $N_e = 80$ shots, (c) $N_e = 10$ shots, (d) $N_e = 2$ 22

Figure 3.2 Imaging experiments using correct velocity model and 10 MHz frequency, with different numbers of near-array receivers of (a) 80, (b) 300, (c) 2,000, (d) 20,000 24

Figure 3.3 Migrated images (b) obtained for correct velocity model (a) 25

Figure 3.4 Migrated images (b) obtained for smooth velocity model (a) 26

Figure 3.5 Migrated images (b) obtained for average velocity model (a) 27

Figure 4.1 Pravec et al. (2002) show results of an asteroid rotation rate study that includes (a) the relationship between the spinning rate distribution and the size of asteroids, (b) the normalization of the spinning rate of small asteroids (0.15 km $<$ D $<$ 10 km) 29

Figure 4.2 (a) Design with the fixed orbit of the transmitter (in black) and receiver satellites (in pink) in the polar coordinate, (b) ground track representation (asteroid reference frame) with a constant spinning rate of an asteroid in the longitudinal direction 30

Figure 4.3 (a) Design with transmitter and receiver satellites in polar orbit with 6,000 hours of acquisition time, (b) shot location at an equator triangular patch with black dots representing shot and pink dots representing receivers, (c) ground track map of the receiver and source location, (d) the top-view (polar) of the source-receiver distribution. . . 32

Figure 4.4 Panels (a)-(d) are the same as in Figure 4.3 except for the shot location is located in the pole, instead of the equator. 33

Figure 4.5 Acquisition design with the fixed orbit of the transmitter and receiver satellites in the polar orbit: shot-record receiver coverage at (a) 1,200 hours of acquisition time, (b) 6,000 hours. Acquisition design with (c) receiver satellite radius increasing from 2.5 km to 3.1 km (with decreasing orbital speed) shows shot-record receiver coverage at 6,000 hours 34

Figure 4.6 3D acquisition designs. For the acquisition time of 6,000 hours, I design 6 possible navigation paths for dual orbiter acquisition. The details (a)-(h) of the acquisition designs are included in Figures 4.7-4.12. 36

Figure 4.7 Design 1. With the fixed orbit of the transmitter satellite, the receiver satellite rotates in the latitudinal direction and alters its orbit in the longitudinal direction. (a) 3D orientation of shifted plane (b) shot location at the equator triangular patch with black dots representing shot and pink dots representing receivers, (c) ground track map of the receiver and source location, (d) the top-view (polar) of the source-receiver distribution. 39

Figure 4.8 Design 2. The receiver satellite alters its orbit in the inclinational (latitudinal) direction with the fixed orbit of the transmitter satellite. Panels (a)-(d) are the same as in the Design 1. 40

Figure 4.9 Design 3. Both the orbits of the receiver and transmitter satellites shift in the longitudinal direction at different revolving rates and directions. Panels (a)-(d) are the same as in the Design 1. 41

Figure 4.10 Design 4. Both receiver and transmitter satellites rotate in the latitudinal direction with different rates and directions of rotation. Panels (a)-(d) are the same as in the Design 1. 42

Figure 4.11 Design 5. The orbit of the receiver satellite shifts in the longitudinal direction and the transmitter shifts in the latitudinal direction. Panels (a)-(d) are the same as in the Design 1. 43

Figure 4.12 Design 6. The transmitter satellite shifts in the longitudinal direction and the receiver satellite shifts in the latitudinal direction. Panels (a)-(d) are the same as in the Design 1. 44

Figure 4.13 Analysis of receiver coordinate coverage for the six acquisition designs (not limited to source location and aperture): (a) rectangular grid representation, where ϕ is the latitude and θ is the longitude in the ground track map, (b) geodesic dome representation. 45

Figure 4.14 80 shot-record receiver coverage: (a) geodesic dome optimized representation, (b) minimization result on the geodesic dome 46

Figure 4.15 80 shot-record midpoint coverage (fold map): (a) geodesic dome optimized representation, (b) minimization result on the geodesic dome . 47

Figure 4.16 Corresponding migrated images (10 shot) obtained by wavefield-based migration using realistic acquisition (a) Design 1 48

Figure 4.17 Corresponding migrated images (1 shot) obtained by wavefield-based migration using realistic acquisition (a) Design 2 49

Figure 4.18 Corresponding migrated images (1 shot) obtained by wavefield-based migration using realistic acquisition (a) Design 3 50

Figure 4.19 Corresponding migrated images (1 shot) obtained by wavefield-based migration using realistic acquisition (a) Design 4 51

Figure 4.20 Corresponding migrated images (1 shot) obtained by wavefield-based migration using realistic acquisition (a) Design 5 52

Figure 4.21 Corresponding migrated images (1 shot) obtained by wavefield-based migration using realistic acquisition (a) Design 6 53

LIST OF TABLES

Table 2.1 Electromangetic parameters for the asteroid model 8

Table 2.2 Attenuation model 10

Table 4.1 Acquisition Designs 37

ACKNOWLEDGMENTS

I still remember walking into the Geophysics Department the first time after traveling 8,000 miles above the Pacific Ocean four years ago. I was excited and full of energy to start my college life at Colorado School of Mines. At the same time, I nervously anticipated all the changes in my life, new experiences, a new culture, and new friends.

I would like to express my deep gratitude to Prof. Paul Sava, my research supervisor, for his patient guidance, enthusiastic encouragement, and useful critique of his research. I would be an entirely different person if Prof. Sava hadn't offered me a wonderful opportunity to conduct research with him and let me be a part of the greatest consortium of all time, CWP. I also would like to express my appreciation to Dr. Robert Grimm, who is the PI for this project and who invited me to collaborate with him. He offered valuable, constructive suggestions during the planning and development of this research work. I have been impressed by his willingness to give his time so generously to me. My grateful thanks are also extended to Dr. David Stillman for his curiosity and questions, which always led to research solutions. I would also like to thank Prof. Roel Snieder for his advice, great conversation at the lunch table, and his support in every way since my freshmen year. The conversation with Dr. Jeff Andrews-Hanna about planetary research problem kept me enthusiastic and encouraged. Prof. Dave Hale taught me my first line of code as well as guided me through the hardest computer class I've ever taken. I am very proud to say that I've completed three of the most difficult seismology classes at Mines with Prof. Ilya Tsvankin. Since my first day at CWP, John Stockwell has been very supportive and helpful in every aspect of life. Shingo Sean Ishida, who is like a dad in the Geophysics Department, ensures our happiness. Pam Kraus takes care of every student in CWP both with life and administrative issues. Without Pam, we would have a hard time. Diane Witters deserves special thanks from me. Diane spends more time with me than anyone else. My language barrier has been overcome

by her glad assistance. I cannot imagine how I could finish my thesis without her support. Not only her help in writing, but also her encouragement in my life always cheers me up when I feel down. Her hard work and greatness will pay off and I will never let her down.

Last but not least, the Geophysics Department has given room for me to grow both intellectually and socially. I have great gratitude for Prof. Terry Young, the Geophysics Department Head, who has made this place a welcoming and learning environment for me. Michelle Szobody has helped me through the process of getting my degree in four years. Without her, I would not be able to complete this degree. Dawn Umpleby, who I met the first day of school, has always been there for me and has made me smile and happy every time I walk into the Geophysics Department.

I am very thankful for all the mindful and wonderful people I met at Colorado School of Mines. Johannes Douma, who first introduced me to Geophysics, struggled and learned with me throughout our undergraduate and graduate degrees and has been a great motivation for me to learn and strive for the best. Without Esteban Diaz, who has always been a master of coding for me, my code would not run and my thesis would not be complete. During the last semester, I have struggled with research and life. Satyan and my best roommate, Vladimir Li, always take care of me and support me anyway they can. Without all of my CWP friends, my life mostly at night would be very quiet and hard. I am also glad that I was a part of resident life for two years at Mines. I will miss all those experiences and happiness that I had with all my RA friends and floor residents.

I will miss all the Thai friends that I have met in Colorado: Mod, P'nut, Imm, Pete, Huge, King, Joe, Earth, P'hong, P'pump, Nut, Petch, P'amp, and others. You have made my four years in the United States like home in Thailand. Finally, I wish to thank my parents and family for their support and encouragement throughout my study.

This work was supported by the NASA Planetary Instrument Definition and Development Program, grant number NNX11AJ50G (PI R. Grimm) and by the sponsors of the Center for Wave Phenomena at Colorado School of Mines. The reproducible numeric examples in this

paper use the Madagascar open-source software package (Fomel et al., 2013) freely available from http://www.ahay.org.

CHAPTER 1

INTRODUCTION

Asteroids and comets give primary evidence of the composition and dynamic, collisional, and thermal evolution of the early Solar System (Bottke et al., 2002; Festou et al., 2004). The interior structure of asteroids and comets holds the key for understanding the differentiation, impact, disruption, and reassembly history of the early planetary processes (Binzel et al., 2003). Near-Earth Objects (NEOs) are of main interest for space investigation because of their possible collision risk with Earth (Chapman, 2004) and because they are accessible to exploration, e.g. with the robotic Asteroid Retrieval Mission (ARM) proposed by NASA in 2010 (Brophy et al., 2012).

The interior of asteroids and comets is considered a complex target. Many geophysical methods such as the gravity method (Hilton, 2002), the magnetic method, and electromagnetic (EM) induction sounding (Grimm, 2009) are possible instruments for exploration, but their limitations prevent successful imaging of small interior objects. Wavefield methods such as seismic (Sheriff and Geldart, 1995) and electromagnetic wave propagation, e.g., ground penetrating radar (GPR) (Daniels, 2004), offer the highest resolution for imaging the complex internal structure of asteroids and comets.

In this thesis, instead of discussing seismic methods, which are limited by the fact that their sensors and instruments need to be coupled with the target surface (Henrique et al., 1999; Huebner and Greenberg, 2001; Walker et al., 2006), I implement radiowave (radar) exploration. The radar techniques appear to be simple, effective, and feasible in terms of acquisition and imaging design primarily because they do not require instruments in direct contact with the studied object. Radiowave acquisition can be separated into two experimental setups: transmission and reflection. The transmission experiment takes place when the electromagnetic wave propagates through the medium and is recorded at the opposite

side of the internal surface. In the reflection experiment, the wave propagates inside the target, reflects at discontinuities inside the structure under investigation, and gets recorded back at the source location. The transmission and the reflection experiments are comparable to the tomography and surface imaging experiments in seismic, respectively.

The feasibility of using transmission data for tomography and reflection data for imaging asteroids and comets has been presented by Safaeinili et al. (2002) and Richardson et al. (2002). The Comet Nucleus Sounding Experiment by Radio wave Transmission (CONSERT) of the Rosetta mission (Kofman et al., 2007) will conduct an internal imaging project using transmission traveltime tomography on the comet 67P/Churyumov-Gerasimenko. The CONSERT experiment seeks to run tomography experiments using different source locations provided by a moving orbiter and a stationary receiver attached to the the comet (Kofman et al., 2007). Even when using reflected data from the internal structure to improve the image quality, the resolution of the internal imaging is still limited because of the single receiver (Barriot et al., 1999; Benna et al., 2004).

Sava et al. (2014) and Grimm et al. (2014) compare single-orbiter acquisition with dual-orbiter acquisition and the corresponding imaging in 2D. They demonstrate that multiple orbiters, rather than a single orbiter, offer a variety of illumination and thus provide better resolution for reflection imaging. The dual-orbiter acquisition creates multi-offset data that enhances the signal-to-noise ratio over single-offset imaging. Therefore, in this thesis, I focus my attention on 3D imaging using dual-orbiter acquisition, and do not discuss the alternative single-orbiter setup.

In the following, I introduce the 3D acquisition and navigation design of the dual-orbiter experiment, demonstrate the ideal scenarios for 3D acquisition, and generate 3D images of an asteroid using both hypothetical setups and realistic orbits. I show the navigation and acquisition tools required for determining the needed acquisition time during the dual-orbiter experiment and show the corresponding internal images resulting from different experiment configurations. The electromagnetic properties of the asteroid model and the sensitivity of

the velocity model in 2D are already discussed in the paper by Grimm et al. (2014). In this thesis, I address the following research questions:

- What is a suitable experimental setup for 3D imaging of an asteroid target?
- What type of wave equation can be used for forward modeling and how can I incorporate attenuation effects (caused when electromagnetic waves propagate inside the conductive media) into this equation?
- What are the optimal navigation parameters and designs to maximize 3D data coverage for dual-orbiter acquisition? What are the limitations for obtaining full coverage? What are the tradeoffs between acquisition cost and the quality of migrated images?
- What factors determine good quality images in shot-record migration?
- What is an acceptable signal-to-noise ratio in the migrated images?
- Given the same limited survey time and resources, what criteria can one use to select the best 3D acquisition design? How does the migrated image obtained from sparse and irregular realistic acquisition compare with the image obtained using an ideal acquisition design with uniform and dense data coverage?

CHAPTER 2

3D ELECTROMAGNETIC WAVE EQUATION MODELING

The Telegraph equation is a diffusive electromagnetic wave equation that is derived from Maxwell's equations, illustrating the foundational ideas behind classic electrodynamics. Under the assumption of free charges and currents, I derive the scalar-telegraph electromagnetic equation that is used in the 3D modeling section.

2.1 Electromagnetic wave equation and finite difference scheme

Maxwell (1861) presented four partial differential equations that describe how an electric field can be created by a change in a magnetic field and vice versa. Electric and magnetic fields can also be created by existing charges and currents (Lorrain and Corson, 1962). The first of these equations, Gauss's law, relates the distribution and quantity of electric charges to the magnitude of the electric field as shown in

$$\nabla \cdot \mathbf{E} = \frac{1}{\varepsilon_0}\rho, \tag{2.1}$$

where $\mathbf{E}$ is the electric field, ρ is the electric charge, and ε_0 is the electric permittivity of space.

The second equation shows that since magnetic fields propagate perpendicular to the electric field direction, which is parallel to the gradient of the electric field direction, the divergence of magnetic fields is zero:

$$\nabla \cdot \mathbf{B} = 0, \tag{2.2}$$

where $\mathbf{B}$ is the magnetic field.

The third equation, Faraday's law, is the generalization of electromagnetic induction and relates the time-varying magnetic fields to the spatially-varying electric fields as shown in

$$\nabla \times \mathbf{E} = -\frac{\partial \mathbf{B}}{\partial t}. \tag{2.3}$$

Finally, Ampere's law connects the magnetic field that is generated by currents and the time-varying electric field as shown in

$$\nabla \times \mathbf{B} = \mu_0 \mathbf{J} + \mu_0 \varepsilon_0 \frac{\partial \mathbf{E}}{\partial t}, \tag{2.4}$$

where μ_0 is the magnetic permeability and $\mathbf{J}$ is the electric current quanity. In this representation of Maxwell's equations, the electric field is generated by a charge (ρ) or by the changing magnetic field ($\partial \mathbf{B}/\partial t$). Similarly, the magnetic field can be induced by a current ($\mathbf{J}$) or by the changing electric field ($\partial \mathbf{E}/\partial t$) (Griffiths, 2008).

In a vacuum or charge-free space, an inhomogeneous electromagnetic wave equation is created under the assumption of neither charges (ρ) nor currents ($\mathbf{J}$), and dielectric permittivity (ε) of the medium is varying in space, but the magnetic permeability (μ) of the medium is constant. Using Faraday's law (equation 2.3), one substitutes the magnetic fields ($\mathbf{B}$) with $\mu \mathbf{H}$, where $\mathbf{H}$ is the strength of the magnetic field or auxiliary magnetic field, to obtain

$$\nabla \times \mathbf{E} \quad = \quad -\mu \frac{\partial \mathbf{H}}{\partial t}. \tag{2.5}$$

Applying the curl operation to both sides of equation 2.5 yields

$$\nabla \times (\nabla \times \mathbf{E}) \quad = \quad \nabla \times \left(-\mu \frac{\partial \mathbf{H}}{\partial t} \right). \tag{2.6}$$

Next, I apply the vector calculus identity $\nabla \times (\nabla \times \mathbf{E}) = \nabla (\nabla \cdot \mathbf{E}) - \nabla^2 \mathbf{E}$, swap the space and time derivatives, and take μ outside the derivatives under the assumption that different medium materials respond to the same degree of magnetization, assuming μ is constant in space or $\nabla \mu = 0$. Then equation 2.6 simplifies to

$$\nabla (\nabla \cdot \mathbf{E}) - \nabla^2 \mathbf{E} \quad = \quad -\mu \frac{\partial (\nabla \times \mathbf{H})}{\partial t}. \tag{2.7}$$

Under the assumption of free charges and currents, $\nabla \cdot \mathbf{E} = 0$; then one substitutes $\nabla \times \mathbf{H}$ with $\varepsilon \partial \mathbf{E}/\partial t + \sigma \mathbf{E}$ in equation 2.7 to obtain

$$-\nabla^2 \mathbf{E} \quad = \quad -\mu \frac{\partial}{\partial t} \left(\varepsilon \frac{\partial \mathbf{E}}{\partial t} + \sigma \mathbf{E} \right), \tag{2.8}$$

which can also be re-arranged in the form of the Telegraph equation:

$$\nabla^2 \mathbf{E} - \mu\varepsilon \frac{\partial^2 \mathbf{E}}{\partial t^2} - \mu\sigma \frac{\partial \mathbf{E}}{\partial t} = 0. \tag{2.9}$$

The parameters controlling this wave equation are electric permittivity (ε), which measures the electric field that is generated per charge in the dielectric medium; magnetic permeability (μ) , which indicates the level of magnetization of the medium; and conductivity (σ), which determines the attenuation of the propagating waves.

The scalar imaging method (successfully implemented in remote sensing and seismic experiments) is an established means for processing ground penetrating radar (GPR) data (Grasmueck, 1996; Johansson and Mast, 1994; Lopez-Sanchez and Fortuny-Guasch, 2000). To accurately model GPR wave propagation and scattering, one must take into account the characteristic of the antenna radiation and vectorial nature of the radar wave i.e., angle-dependent amplitude and polarization variations (Annan et al., 1975; Kruk et al., 2003). Because the electromagnetic and elastic wave equations share many similarities in term of wave propagation kinematics (e.g., propagation time, medium velocity, and reflection an ad diffraction responses at discontinuities), GPR imaging using the scalar wave assumption is possible (Fisher et al., 1992). Unfortunately, the scalar-imaging approach cannot correctly retrieve polarization and interface partitioning information of a radar wave.

However, there are number of techniques that use scalar imaging and include the antenna radiation characteristic in GPR data processing. Example of these techniques are pseudoscalar wavefield using 3D Kirchhoff time-migration scheme (Moran et al., 2000) and Slipt step Fourier migration (Sena et al., 2003). In this thesis, I investigate the 3D imaging that dominately depedends on the interior geometry (reflectivity) of an asteroid target.

For the wave modeling scheme, I employ the time-domain electromagnetic Telegraph equation, which resembles an acoustic equation with the addition of the diffusion term, including electric permittivity, magnetic permeability, and conductivity parameters in the equation.

Under the assumption that the changes in wave polarization at interfaces (especially curved interfaces) are small, it is possible for the scalar representation of electric fields in the Telegraph equation to preserve the kinematics of the wave equation. However, the dispersion effect is much more severe with radar than with seismic due to conductivity and the influence of dielectric relaxation. Thus, I assume that I can utilize the Telegraph equation (2.10) to characterize the kinematic of the wave equation using a scalar wavefield (E) as shown in

$$\nabla^2 \mathrm{E} = \mu\sigma \frac{\partial \mathrm{E}}{\partial t} + \mu\epsilon \frac{\partial^2 \mathrm{E}}{\partial t^2}. \tag{2.10}$$

Then, when I substitute the partial derivatives with finite differences, I obtain the equation

$$\nabla^2 \mathrm{E} = \mu\sigma \left(\frac{\mathrm{E}_+ - \mathrm{E}_-}{2\left(\Delta t\right)} \right) + \mu\epsilon \left(\frac{\mathrm{E}_+ - 2\mathrm{E} + \mathrm{E}_-}{\left(\Delta t\right)^2} \right), \tag{2.11}$$

where E_+ is the scalar electric field at the forward time step $(t+1)$, E is the electric field at the current time step (t), and E_- is the electric field at the backward time step $(t-1)$. Algebraic simplifications lead to

$$\frac{\left(\Delta t\right)^2 \nabla^2 \mathrm{E}}{\mu\epsilon} = \frac{\sigma\left(\Delta t\right)}{2\epsilon} \left(\mathrm{E}_+ - \mathrm{E}_-\right) + \mathrm{E}_+ - 2\mathrm{E} + \mathrm{E}_-, \tag{2.12}$$

and after rearranging the terms, I obtain

$$\mathrm{E}_+ = \frac{2}{\left(1 + \frac{\sigma(\Delta t)}{2\epsilon}\right)} \mathrm{E} - \frac{\left(1 - \frac{\sigma(\Delta t)}{2\epsilon}\right)}{\left(1 + \frac{\sigma(\Delta t)}{2\epsilon}\right)} \mathrm{E}_- + \left(\frac{\left(\Delta t\right)^2}{\left(1 + \frac{\sigma(\Delta t)}{2\epsilon}\right)\mu\epsilon} \right) \nabla^2 \mathrm{E}. \tag{2.13}$$

This form of the Telegraph equation implies that the propagating wavefield is attenuated in space, and the attenuation does not depend on frequency. The diffusion term attenuates the wavefield in a conductive medium. Thus, when conductivity(σ) is zero and $\mu\epsilon = 1/v^2$, then the electromagnetic finite difference model is acoustic.

2.2 3D model building

I test my finite-difference simulation of wave propagation in a 3D model based on asteroid Eros 433 (Gaskell, 2008) with dielectric parameters using a 3D synthetic asteroid model provided by Grimm et al. (2014). The model is scaled down from the Eros geometry of

34.4 x 11.2 x 11.2 km^3 to 1 x 0.3 x 0.3 km^3. The asteroid model is similar to the OSIRIS-Rex mission target, 101955 Bennu (Nolan et al., 2013).

For an imaging study, the interior structure of a synthetic asteroid model is considered a rubble pile (Richardson et al., 2002; Weissman et al., 2004) with monolithic (fine-grained) rock or ice materials. The model also consists of fractures and blocks of rock in situ (Richardson et al., 2002). With the two components of rubble piles and rocks, the size-frequency distribution (SFD) of the internal structure can provide clues about the collisional history of an asteroid (Durda et al., 2007; Leinhardt et al., 2000; Michel et al., 2004).

The interior structure of the model consists of varying sizes of spherical objects (representing rock) simulated using the geometric algorithm of Tanga et al. (1999). The interior of the model has 50% rock fragments and 50% regolith (loose material). Grimm et al. (2014) assume that the rock fragments have a density of 3.0 g/cm^3 and the regolith has a density of 1.0 g/cm^3. The asteroid model then has a bulk density of 2.0 g/cm^3, which is the same as the mean S and C types of asteroid bulk density (Carry, 2012).

Table 2.1: Electromangetic parameters for the asteroid model

	Rock	Regolith	Space	units
d	3.00	1.00	0	g/cm^3
ϵ'	6.86	1.93	1	-
v	0.11	0.22	0.30	m/ns
μ_0	1.25	1.25	1.25	10^{-6} H/m
σ	0.001	0.0005	0	S/m

The wave velocity can be calculated by converting the density to a relative dielectric constant $\epsilon' = \epsilon_r/\epsilon_0 = 1.93^{\mathrm{d}}$ using the relationship developed for lunar rocks by Olhoeft and Strangway (1975), and $\epsilon' = 1.93$ is obtained for regolith and 6.86, for rock, where ϵ_0 is the dielectric permittivity of space. The electromagnetic velocity is $v = 1/\sqrt{\mu_0\epsilon_r} = 1/\sqrt{\mu_0\epsilon_0\epsilon'}$, $\epsilon_0 \approx 8.85\text{x}10^{-7}$ F/m, and the magnetic permeability of space (μ_0) $\approx 1.25\text{x}10^{-6}$ H/m; the result is $v_{\mathrm{rock}} = 0.11$ m/ns and $v_{\mathrm{regolith}} = 0.22$ m/ns, as shown in Table 2.1.

The model also has different conductivity values that control the model attenuation. Electromagnetic waves are attenuated due to wave-scattering from medium dielectric differences and to intrinsic absorption (Grimm et al., 2006). The attenuation from structures that are larger than the wavelength, e.g., dielectric contrasts, are detected from wave modeling; the attenuation from structures that are smaller than a wavelength and the intrinsic absorption can be calculated using a loss tangent $\tan\delta$. The attenuation calculation relates to the skin depth measurement, $\tan\delta = \mathrm{v}/\pi f s = \lambda/\pi s$, where f is the frequency, λ is the wavelength in the object, and s is the skin depth (Grimm et al., 2006).

For chondritic asteroids, Heggy et al. (2006) calculate $\tan\delta < 0.005$ from 10-100 MHz frequency. Thus in this case, scattering dominates the attenuation in the medium. Using the 20-25 MHz of GPR attenuation studies conducted by Grimm et al. (2006) and the 20 MHz orbital radar penetration studies by Stillman and Grimm (2011), one can scale $\tan\delta \propto 1/\sqrt{f}$, which is the average between a constant loss tangent (used in the multiple overlapping dielectric loss mechanisms) and $\tan\delta \propto 1/f$ (suitable for constant electrical conductivity). Table 2.2 shows the frequency-dependent attenuation (for 5, 10, and 15 MHz) that is calculated from the above formulation. In this thesis, I use 10 MHz for the source frequency and its corresponding attenuation (for high, medium, low, and very low), which are listed in the middle column of Table 2.2. Since, the level of attenuation is proportional to the conductivity in an object medium, I can calculate the correct model conductivity and input this parameter into a wavefield reconstruction step, which is discussed in Chapter 3, to take the attenuation effect into account.

The velocity and the electromagnetic parameters (e.g., the attenuation model of space, regolith, and rock) are also used in the model following Grimm's assumptions about the physical property of an asteroid. Further discussion about the 3D model building can be found in the paper by Grimm et al. (2014).

In this thesis, I perform wavefield modeling with a seismic Ricker wavelet with a center frequency of 10 MHz. The 10 MHz frequency is in the range of existing space exploration

Table 2.2: Attenuation model

Case	5 MHz	**10 MHz**	15 MHz
Very Low	$3.2\text{x}10^{-6}$	$\mathbf{3.20\text{x}10^{-6}}$	$3.2\text{x}10^{-6}$
Low	$3.6\text{x}10^{-5}$	$\mathbf{4.85\text{x}10^{-5}}$	$6.1\text{x}10^{-5}$
Medium	$1.1\text{x}10^{-4}$	$\mathbf{1.45\text{x}10^{-4}}$	$1.8\text{x}10^{-4}$
High	$3.6\text{x}10^{-4}$	$\mathbf{4.85\text{x}10^{-4}}$	$6.1\text{x}10^{-4}$

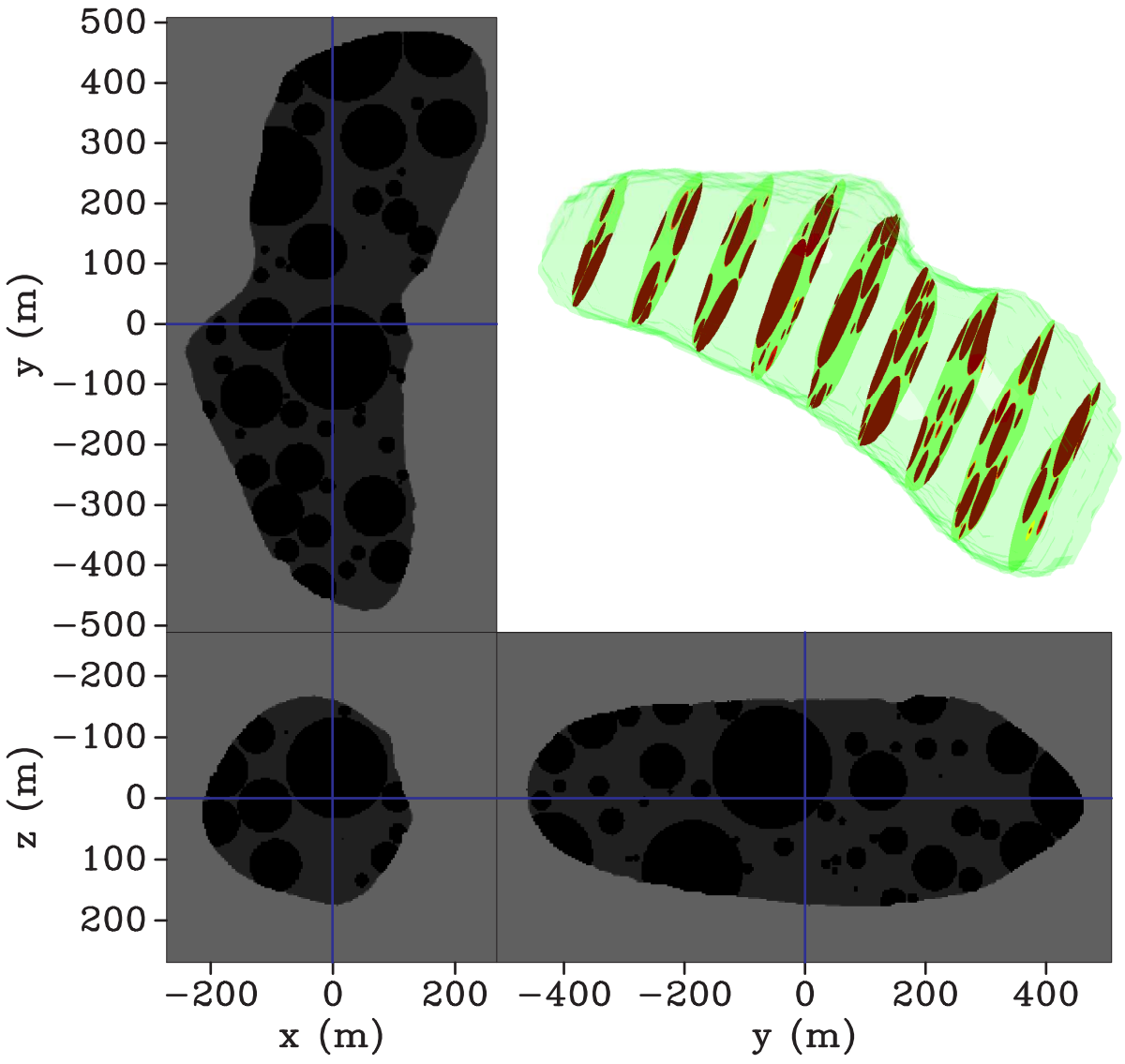

Figure 2.1: 3D synthetic velocity model based on asteroid Eros 433. The model consists of spherical blocks that represent rock fractures (darker color) and the matrix around the rock that represents regolith (softer color). The upper right figure shows 3D slices through the asteroid model in 3D view.

instruments (i.e., Mars Advanced Radar for Subsurface and Ionosphere Sounding (MARSIS: Picardi et al. (2004)) and the 20 MHz Mars Shallow Subsuface Radar (SHARAD: Seu et al. (2007))); the 10 MHz frequency is also in the range of the radio reflection tomography study of Safaeinili et al. (2005). The trade-off relationship between the imaging resolution and the depth of investigation is significant in the electromagnetic survey. The higher the frequency of the wavelet, the better the contrast of the imaging. However, the high frequency source propagates a shorter distance and has higher attenuation effects. With the constant grid size of the asteroid model, the higher frequency wavelet is undersampled and this creates aliasing artifacts. Thus, due to the limits of computational resources, I select the center frequency of 10 MHz, which does not reach the SHARAD-like frequency.

2.3 Wavefield and data

In common seismic exploration, multi-offset data are acquired at multiple receivers (distributed on the ground above the target) for a single transmitter. This variety in data offset creates better illumination of the survey target and improves image quality. However, such an acquisition design is not possible to use with small objects such as asteroids. Hence to mimic the above acquisition, Grimm et al. (2014); Sava et al. (2014) discuss the dual orbiter system design. Instead of a single spacecraft acting as both a transmitter and a receiver, I propose using two spacecrafts that are placed in two different orbiting trajectories and moving at different speeds around the center of the asteroid target. The speed of each orbiting spacecraft can easily be altered by changing the orbiting radius of the spacecraft relative to the asteroid target. Orbiting spacecrafts, acting as transmitters and receivers, would carry radar antennas (with broadband frequency equipment) and generate electromagnetic waves that interact with the target interior. Within the acquisition time, the transmitter revolves around the target and repeatedly comes back to a given location, while the receiver is located each time at a different position, corresponding to the transmitter location. The data (corresponding to a given transmitter location, but with difference receiver locations) is multi-offset and is called shot gathers in seismic exploration. The longer the acquisition

time, the more angles of illumination, resulting in better migrated image quality.

In the 3D realistic acquisition chapter, I show actual 3D designs with realistic survey parameters and address the limitations for getting good data coverage, which determines image quality in the imaging step. Here, I create the ideal 3D acquisition design using a geodesic dome concept to generate transmitter and receiver coordinates for modeling the wavefield and data. Then, I show an efficient technique for modeling wave propagation in a void space. I window the data to obtain the source data, which is located within a 60-degree reflection angle, and then input this information to generate the wavefields (Figure 2.5). Then, I use this reflected data (Figure 2.6) for imaging the asteroid.

Since the image quality depends on the density and distribution of receiver coordinates (as illustrated in the 3D imaging chapter), the geodesic dome is an essential tool for evenly distributing the transmitter and receiver locations on the spherical surface. A network of equilateral triangles form the dome, and the number of triangles is determined by the number of equally distributed coordinates (triangular vertices) on the sphere. The radius of the geodesic dome determines its size and its surface area. With equal distribution of triangles on the sphere, transmitter and receiver coordinates (represented by the midpoints of each triangle) are evenly distributed in the space.

In the ideal acquisition and imaging design, the source geodesic dome has 320 equilateral triangles and the receiver geodesic dome has 80,000 triangles evenly distributed on the sphere. Each geodesic dome has its own set of triangles, and the target triangles (representing source locations) are selected to perform the shot-record experiment. This experiment requires larger area triangles for the transmitter geodesic dome, which is located at a far array at 1.9 km radius, and smaller area triangles for the receiver geodesic dome (near array), which is located at 0.55 km from the asteroid target as shown in Figure 4.21.

With dual-orbiter system, each transmitter is associated with its own set of receivers on the near-array. For the migration step, I restrict the receivers to within a 60-degree aperture.

The following steps comprise the numerical experiments:

- Shift the source using analytic Green's functions from the transmitter (located at 1.9 km) to closer orbits around the asteroid target (located at 0.55 km) (Figure 2.3). This technique reduces the computing time in the void space, since wave analytic Green's functions in void space are fast to compute.

- Simulate wave propagation both toward the asteroid model and reflecting backward from the model using time-domain finite difference modeling with the source location at the closer geodesic dome surface (Figure 2.5). Then, the data are collected at the same closer orbits (near array) (Figure 2.6).

- Relocate the acquired wavefields, using the analytic Green's function, from the near-array orbits to the receiver locations.

In this chapter, I use electromagnetic waves similar to existing radar-system instruments (Kofman et al., 2007) in space. The time-domain electromagnetic Telegraph equation is implemented to explain the wave propagation with the scalar representation of electric fields. The model parameters, which include dielectric properties and attenuation, are assigned for a 3D imaging experiment. I use a Ricker wavelet with a frequency of 10 MHz under the assumption that such radar instruments can transmit and record broadband waveforms. Then, I generate multi-offset data from reflection experiments with a dual-orbiter acquisition system. This chapter explains the wavefield recontruction step, which is one of the two components for 3D imaging. In Chapter 3, the multi-offset data is used to reconstruct the interior structure of an asteroid.

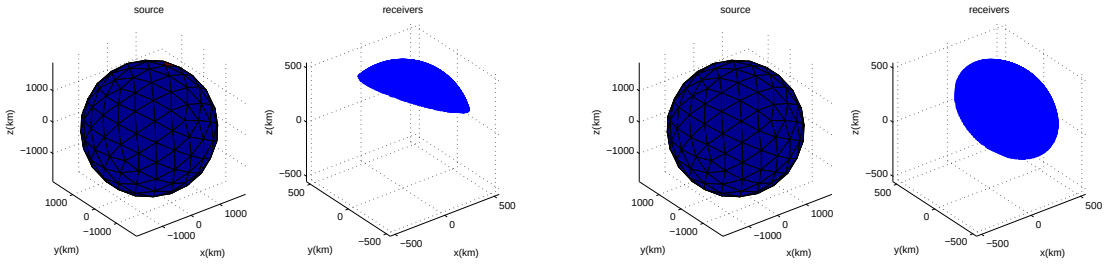

(a)

(b)

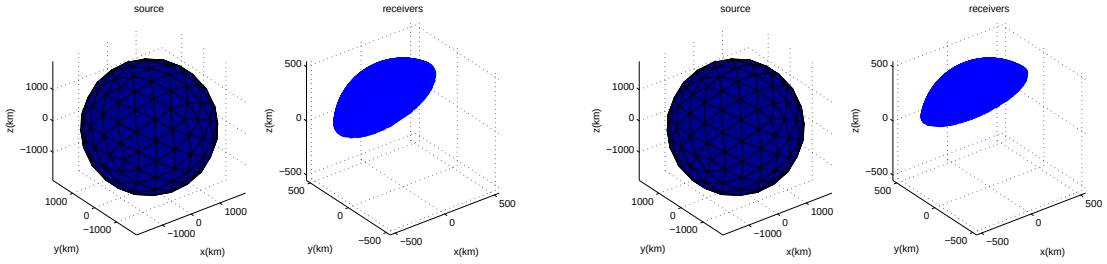

(c)

(d)

Figure 2.2: Shot locations are evenly distributed on the source geodesic dome (1.9 km radius). The receiver geodesic dome is dense and located at a 0.55 km radius. Each shot location has its own shot-record receiver coordinates within a small region corresponding to 60 degrees aperture relative to shots (a) 0, (b) 64, (c) 128, (d) 192

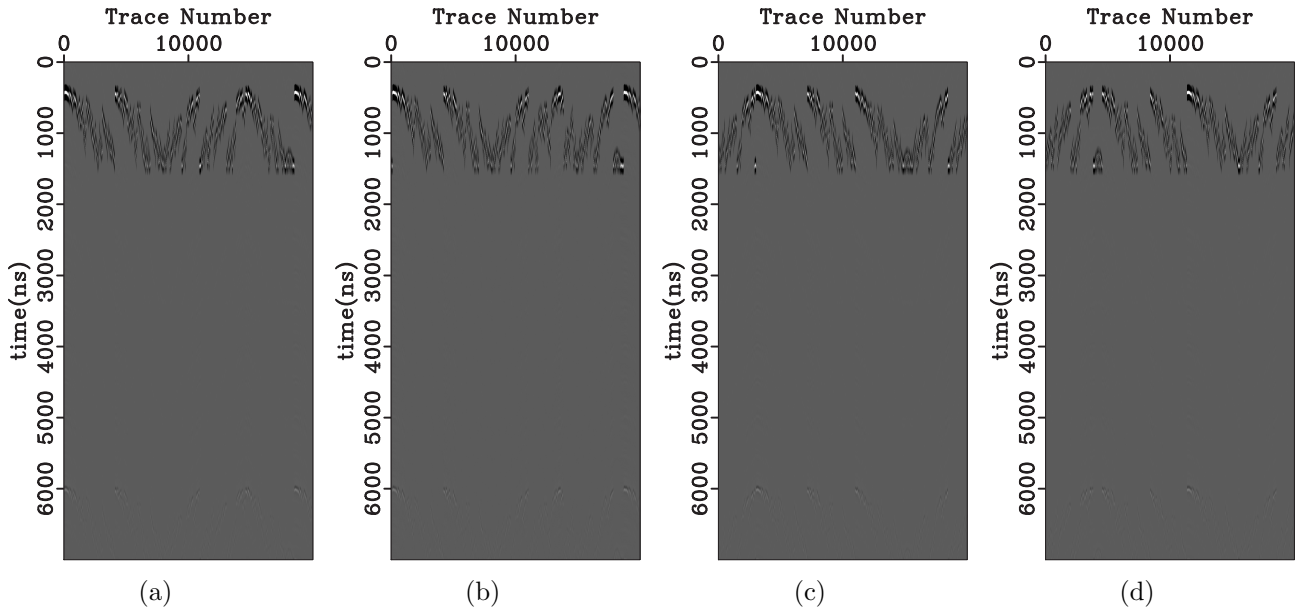

Figure 2.3: Using the analytic Green's function, I shift the source wavelet from the transmitter (located at 1.9 km) to the closer orbits (0.55 km radius) around the asteroid target. The data in panels (a)-(d) correspond to the source and receiver locations shown in the panels of Figure 2.2.

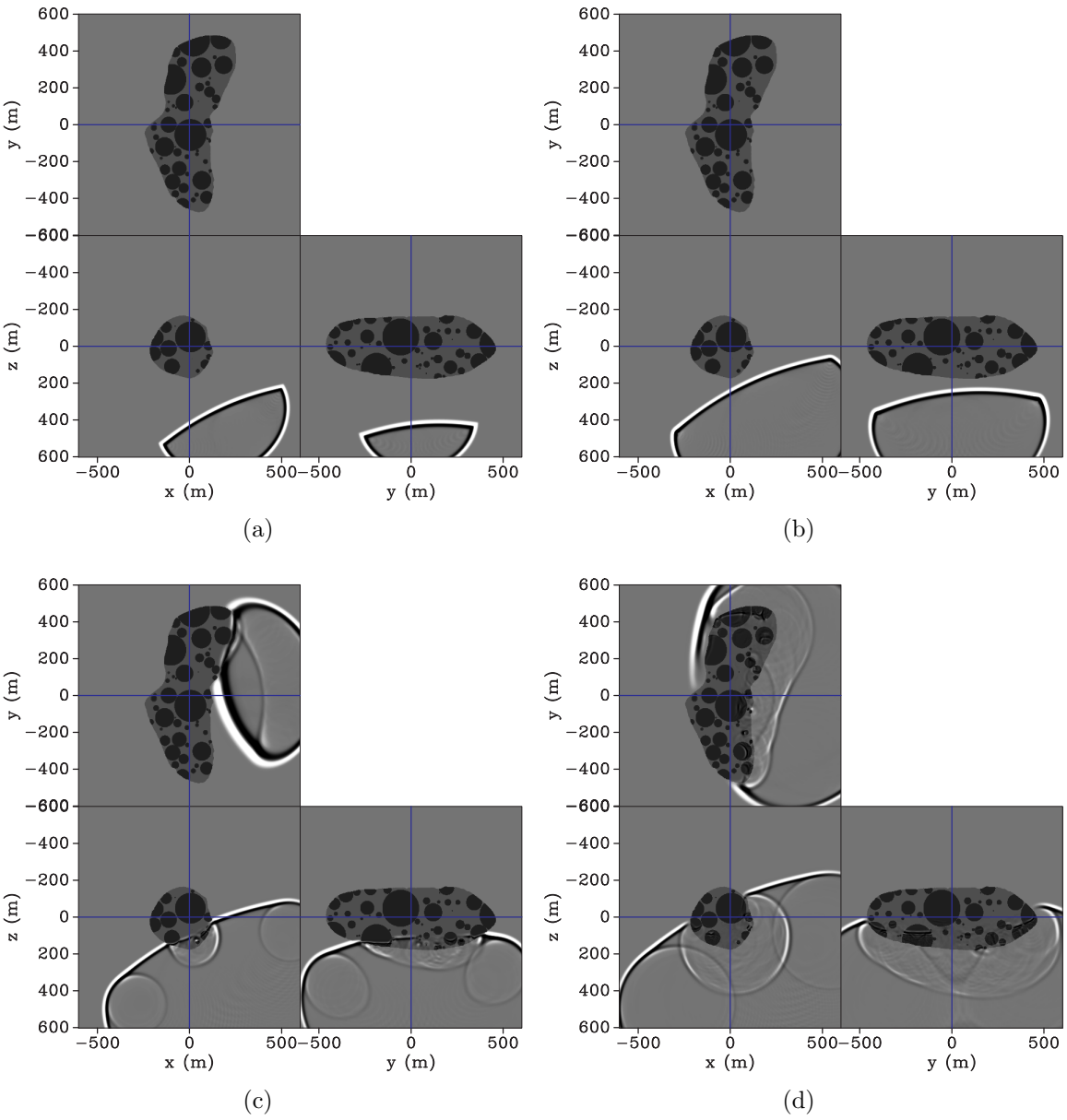

Figure 2.4: Wave propagation using a time-domain electromagnetic finite difference scheme. The wavefield snapshots correspond to the geometry depicted in panel (a) of Figure 2.2 with increments of 1000ns

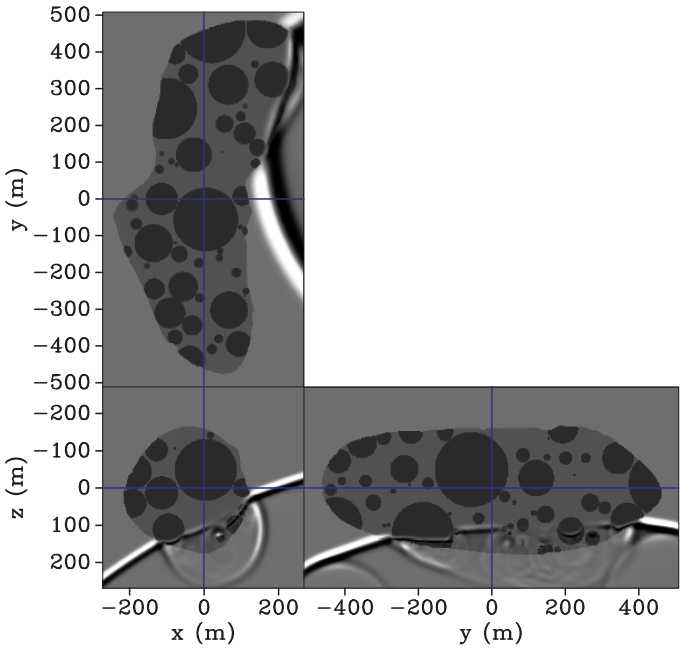

(a)

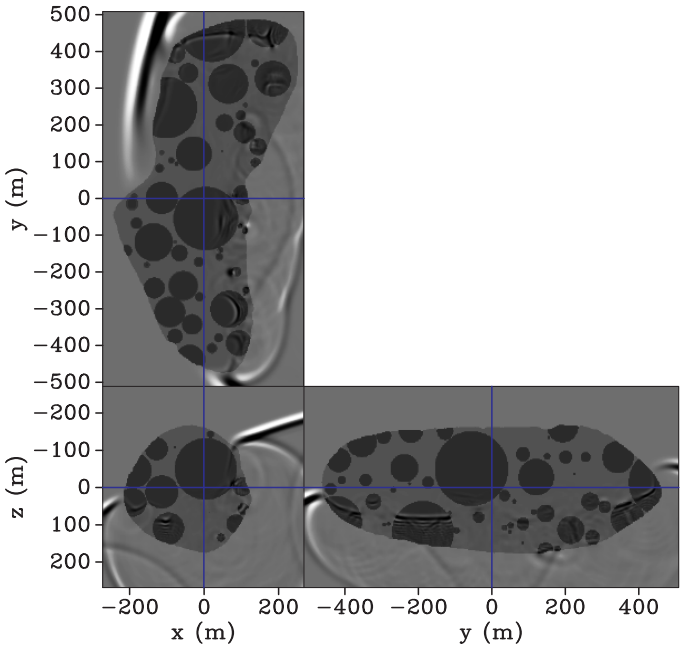

(b)

Figure 2.5: Wavefield snapshots (zoomed in view of Figure 2.4) at panel (a) of Figure 2.2 for time (a) 1000 ns and (b) 1250 ns. These snapshots illustrate the complex and attenuative wavefields when the wave propagates into the asteroid model.

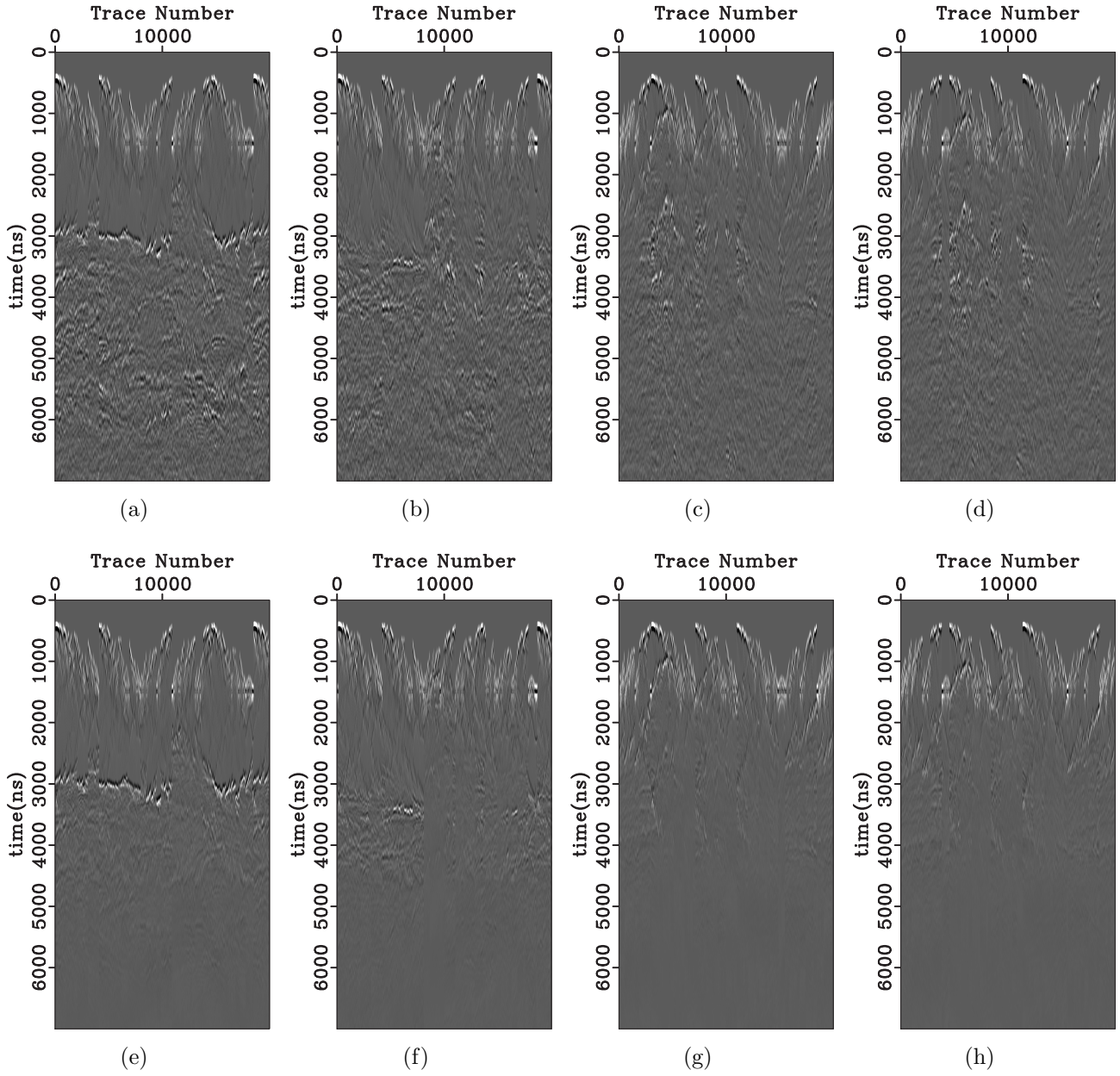

Figure 2.6: Reflected data (collected on receiver geodesic dome) located at 0.55 km radius (near array). In these figures, I show the attenuation effect using different conductivity levels inside the asteroid model. Observed data (without attenuation) correspond to source and receiver coordinates from panels (a)-(d) in Figure 2.2 are shown in (a)-(d), respectively. Observed data (with medium attenuation) are shown in (e)-(h) with respect to source and receiver locations above.

CHAPTER 3

3D IMAGING

In the process of imaging the interior of an asteroid, I use conventional seismic imaging techniques under the assumption of the scalar wavefield and single scattering wave propagation. Such wavefield-based imaging methods have been successfully applied both in seismic exploration (Berkhout, 1984; Claerbout, 1986) and for electromagnetic survey (Miller et al., 2010; Reynolds, 2011).

This wavefield imaging formulation involves two procedures: wavefield reconstruction and application of the imaging condition.

3.1 Wavefield reconstruction and imaging condition

The first element of this imaging method, wavefield reconstruction, is a process that creates wavefields inside the target using the governing wave equation. In Chapter 2, I derive the Telegraph equation (equation 2.10), which accounts for the dielectric parameters (electric permittivity ε and magnetic permeability μ) and the attenuation parameter(conductivity σ). This equation is a special case of the electromagnetic wave equation and explains wave propagation and scattering inside the asteroid:

$$\mathbf{L}(\mu, \varepsilon, \sigma)[\mathrm{E}] = \mu\epsilon\frac{\partial^2 \mathrm{E}}{\partial t^2} + \mu\sigma\frac{\partial \mathrm{E}}{\partial t} - \nabla^2 \mathrm{E} = f(\mathbf{x}, t), \tag{3.1}$$

where $\mathbf{L}$ is a wave operator consisting of dielectric medium parameters, $\varepsilon(\mathbf{x})$ and $\mu(\mathbf{x})$, and attenuation variable $\sigma(\mathbf{x})$, and $\mathrm{E}(\mathbf{x}, t)$ is the wavefield (electric scalar field), which is four-dimensional array of space $\mathbf{x} = \{x, y, z\}$ and time (t). The source function $f(\mathbf{x}, t)$ varies according to space (the position of the transmitter and receiver) and time. The impact of attenuation on the imaging is addressed in Chapter 2.

Here, I define two conventional terms used in wavefield imaging methods: a source wavefield and a receiver wavefield. The source wavefield is the wave that originates at the source

location and propagates toward the target before interacting with interior discontinuities of the target. The receiver wavefield is the reflected wave that originates at subsurface discontinuities, propagates through the medium, and is recorded at the receiver locations. When one uses the correct wave equation that explains wave propagation, any incongruity between the two wavefields demonstrates that the wavefield reconstructions is incorrect and is, in this case, caused by incorrect model parameters.

The source and receiver wavefields, E_s and E_r respectively, are created with the same wave-equation and model parameters. The source wavefield propagates forward in time

$$\mathbf{L}(\mu, \varepsilon, \sigma)[\mathrm{E}_s] = D_s(\mathbf{s}, +t), \tag{3.2}$$

where D_s is a source function at the source location. The receiver wavefield propagates backward in time

$$\mathbf{L}(\mu, \varepsilon, \sigma)[\mathrm{E}_r] = D_r(\mathbf{r}, +t), \tag{3.3}$$

where D_r is received data located at the receiver coordinates.

The second component of this wavefield imaging method, the imaging condition, is an operation which reveals information about the discontinuity inside the target using reconstructed wavefields that were created from wavefield reconstruction (Berkhout, 1984; Claerbout, 1986). With the dual orbiter systems, multi-offset data is acquired from different spacecrafts (transmitters and receivers) and collected from the different propagation paths with varying illumination.

Reflectivity information in space $\mathbf{x} = (x, y, z)$ is calculated using conventional cross-correlation imaging condition of the source and the receiver wavefields in time (Claerbout, 1986) as shown in

$$R_e(\mathbf{x}) \;=\; \sum_t \mathrm{E}_s(\mathbf{x}, t)\, \mathrm{E}_r(\mathbf{x}, t), \tag{3.4}$$

The migrated image from each experiment $R_e(\mathbf{x})$ offers information about the reflector using varied illumination. The summation over shot experiments maximize signal-to-noise

ratio by increasing reflector amplitude and attenuating coherent noise from potential artifacts. This summation leads to a more accurate image of the interior structure:

$$R(\mathbf{x}) = \sum_{e=1}^{N_e} R_e(\mathbf{x}), \tag{3.5}$$

where N_e is the number of experiments.

In the following experiments, I apply the above seismic imaging approach to image the interior of a 3D asteroid. As indicated in the preceding chapter, the sources are placed at 1.9 km from the target origin and are evenly distributed on the spherical surface on a geodesic-dome. The corresponding receivers are selected within the reflection angle (assigned aperture of 60 degrees).

Figure 3.1 shows 3D images obtained with a varying number of experiments (N_e) using medium attenuation, 10 MHz frequency, and the true velocity model. The increasing number of experiments improves image quality. The source geodesic dome (in the upper right of each migrated image) shows even distribution of the source location around the asteroid target. The selected source location is represented by red patches.

The complete experiment allows for 320 shot locations as shown in Figure 3.1(a). The corresponding migrated image for the complete experiment demonstrates a high signal-to-noise ratio of the asteroid target. With the medium attenuation of rock and regolith, the wavefield is attenuated before reaching the center of the asteroid, resulting in an unclear structure inside the asteroid target. For the two-shot experiment, as shown in Figure 3.1(d), the migrated image represents one illumination angle at the source location and fails to give a good interpretation of this 3D image.

3.2 Migrated image quality using varied receiver coverage

The coverage and density of the shot-record receivers determine the migrated image quality. The greater the number of receivers, the higher the signal-to-noise ratio resulting during the imaging condition. In the ideal acquisition design, I use a geodesic dome with evenly spaced and dense patches to create good receiver coverage. Near-array receiver coordinates

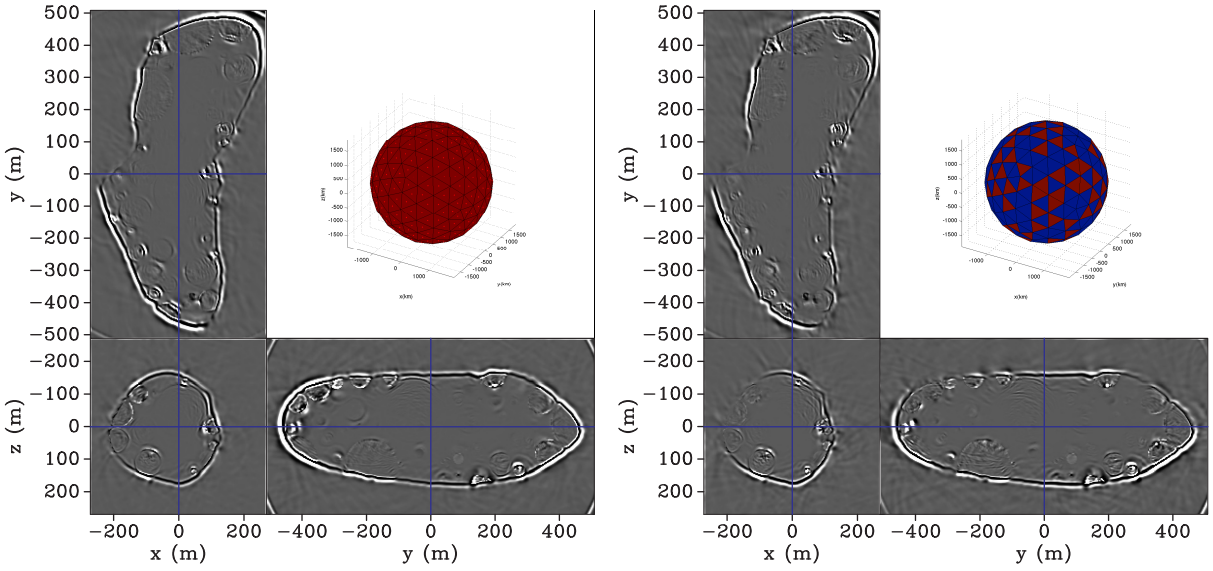

(a)

(b)

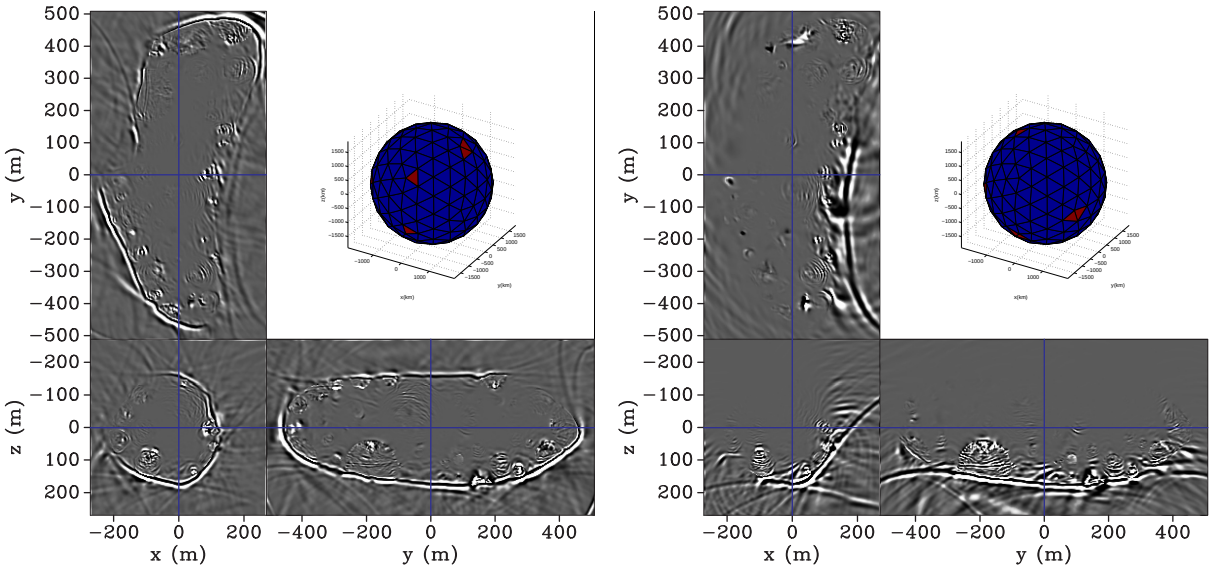

(c)

(d)

Figure 3.1: Imaging experiment using 10 MHz frequency, true velocity mode, medium attenuation, dense and evenly distributed receiver coverage: (a) migrated images with complete acquisition ($N_e = 320$ shots), (b) $N_e = 80$ shots, (c) $N_e = 10$ shots, (d) $N_e = 2$

are evenly distributed on the receiver geodesic dome, but as I discuss in the next chapter, in realistic acquisition, the shot-record receiver coordinates are sparse and randomly distributed on the sphere, which downgrades the migrated image quality.

Here, I evaluate imaging quality for a variable number of receivers on the near array as exhibited in Figure 3.2(a)-(d). In each migrated image, the receiver coverage is shown in the upper right corner. For migration, the receivers are selected within the 60-degree aperture of the reflection angle.

A comparison of the migrated image using 20,000 receivers (Figure 3.2(d)) vs. those using 300 receivers (Figure 3.2(a)) shows clearly that the image quality directly depends on the number of receivers. However, in Chapter 4, I demonstrate that creating good coverage with a high number of receivers to perform 3D imaging is impossible with the limited acquisition time and restricted survey parameters.

3.3 Migrated image quality using different velocity models

An important factor that determines the migrated image quality is the correctness of the velocity model used for the wavefield reconstruction shown in equation 3.1.

In this demonstration, the migrated images (Figure 3.3-3.5 (a)) are generated based on the synthetic velocity models (Figure 3.3-3.5 (b)). The migrated image using the true velocity model shows the best image of the interior structure of an asteroid. In contrast, the migrated images using incorrect velocity models (smooth and average velocities) fail to show the reflectivity of the asteroid interior (Figure 3.5). In an actual exploration, the velocity model is unknown prior to the survey. In this thesis, I focus on applying imaging methods using the reflection data to image the interior of the asteroid in 3D assuming that the velocity model is known. Alternatively, with the dual orbiter systems, wavefield tomography can provide insight about velocity information using multi-offset transmission data (Plessix, 2006; Pratt and Worthington, 1990; Tarantola, 1984)

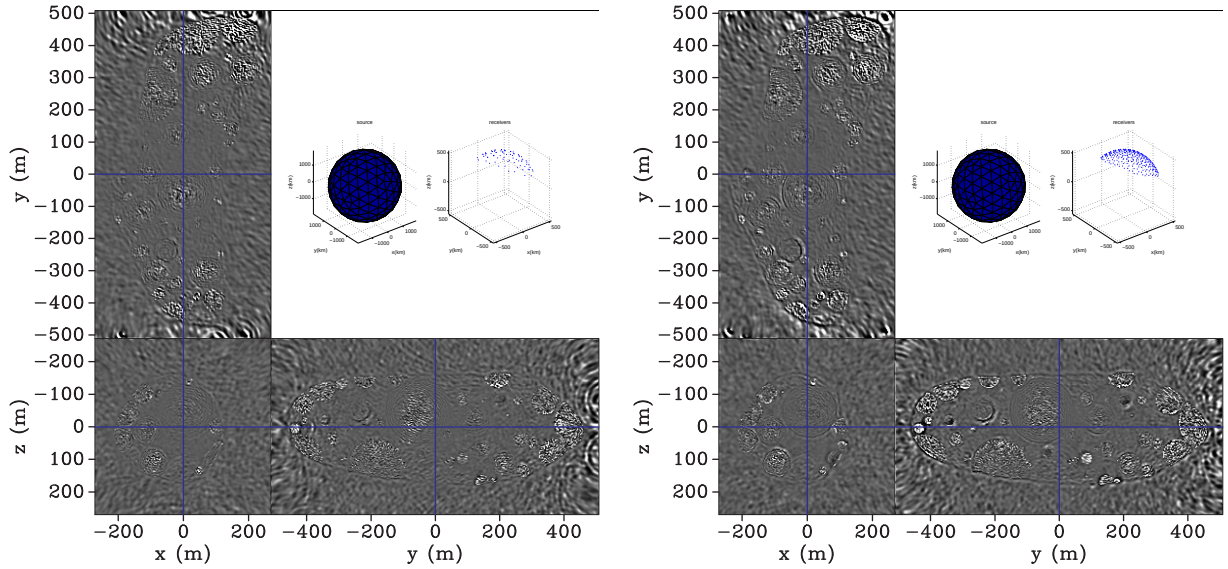

(a)

(b)

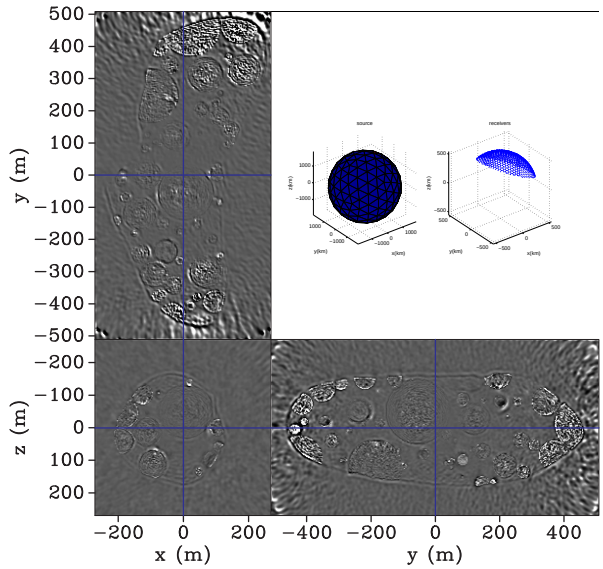

(c)

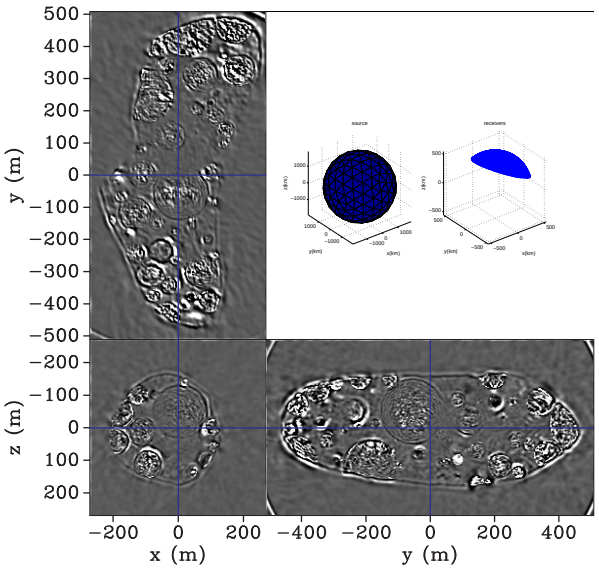

(d)

Figure 3.2: Imaging experiments using correct velocity model and 10 MHz frequency, with different numbers of near-array receivers of (a) 80, (b) 300, (c) 2,000, (d) 20,000

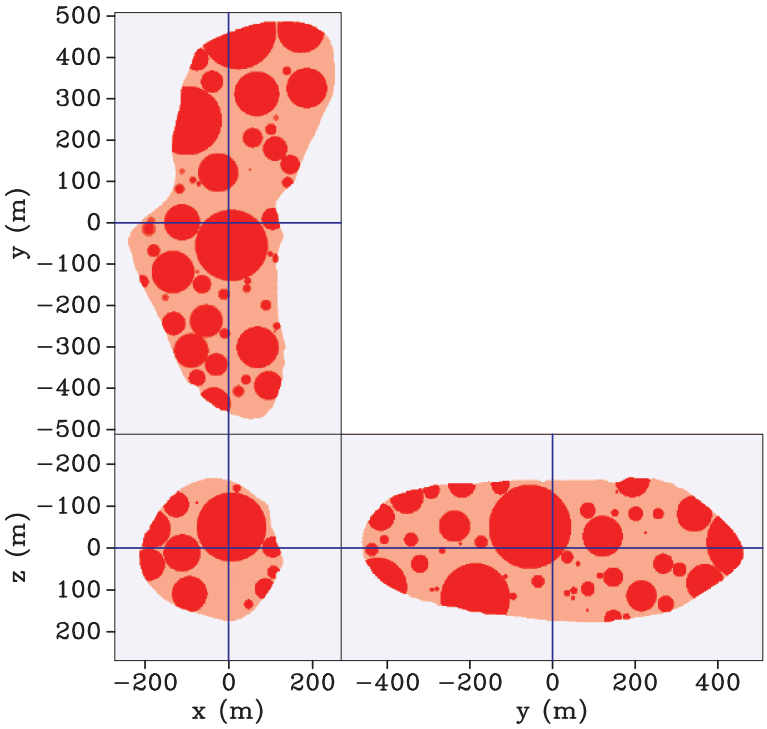

(a)

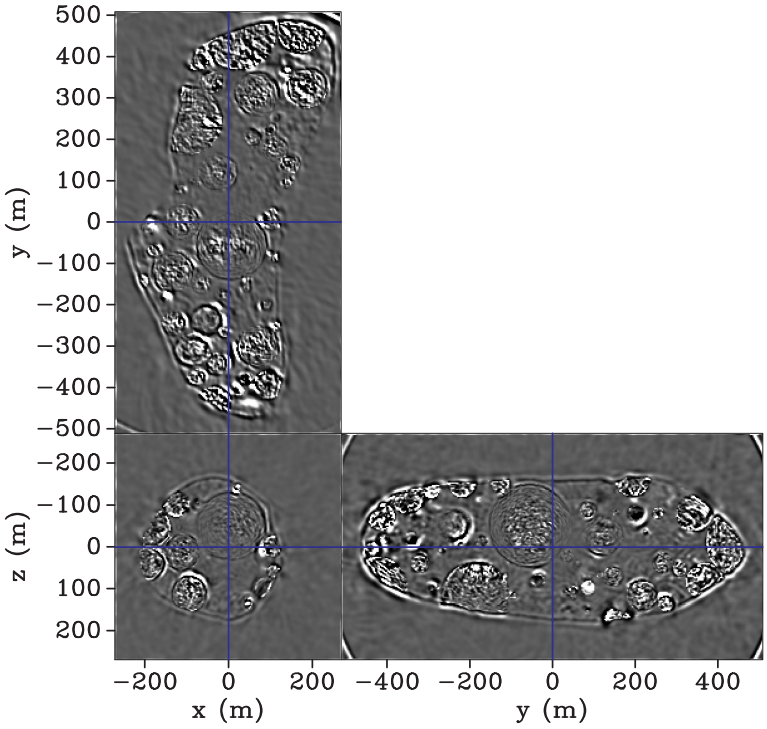

(b)

Figure 3.3: Migrated images (b) obtained for correct velocity model (a)

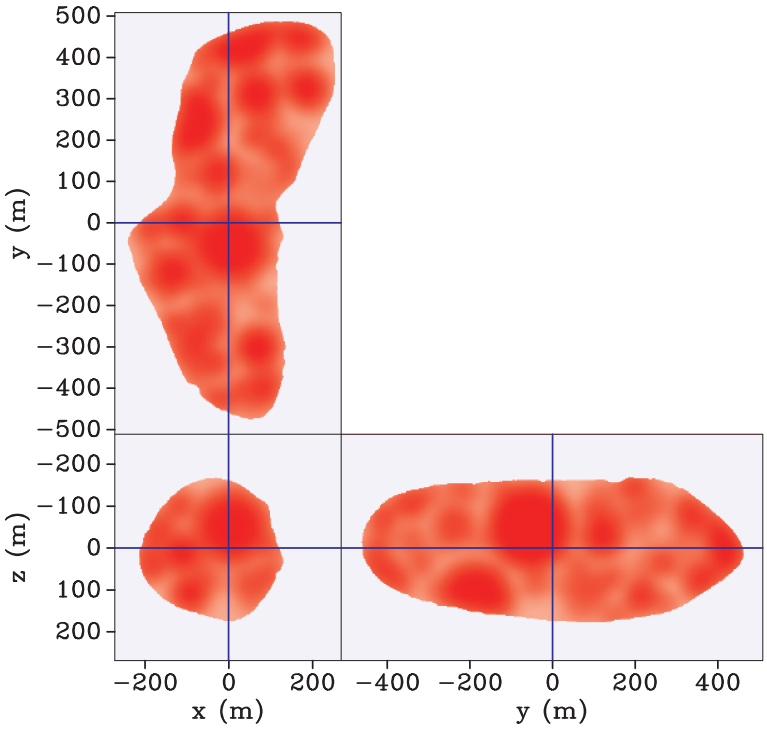

(a)

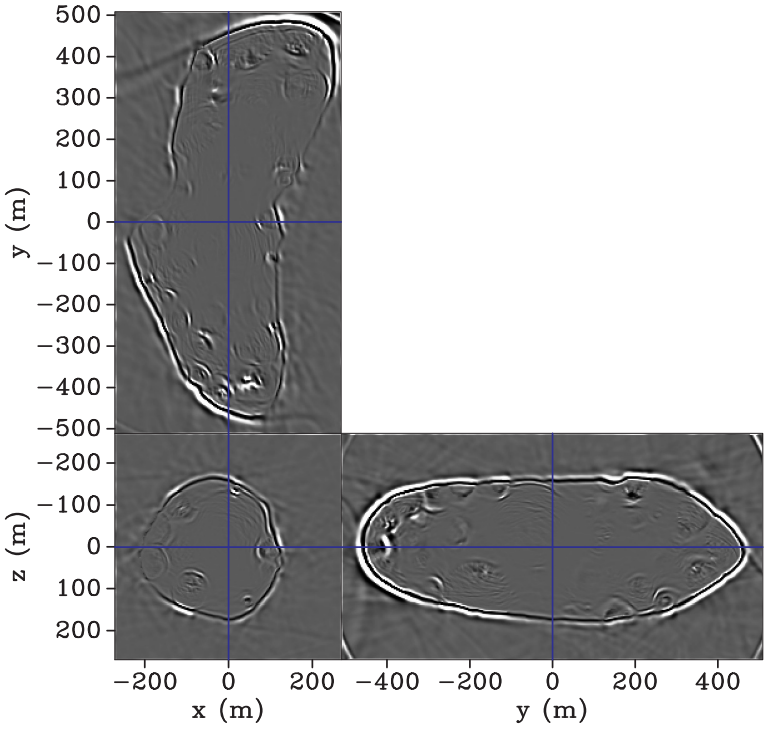

(b)

Figure 3.4: Migrated images (b) obtained for smooth velocity model (a)

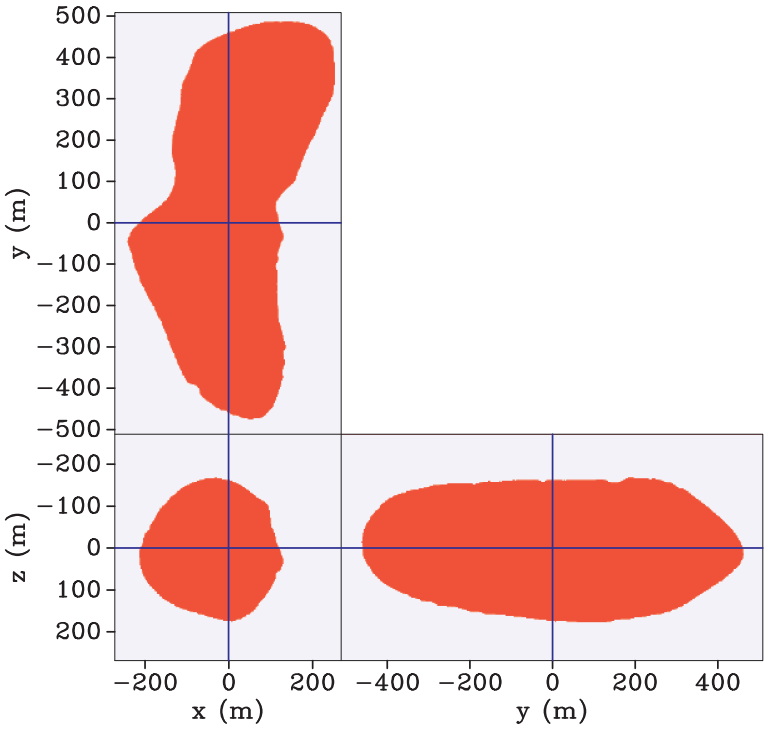

(a)

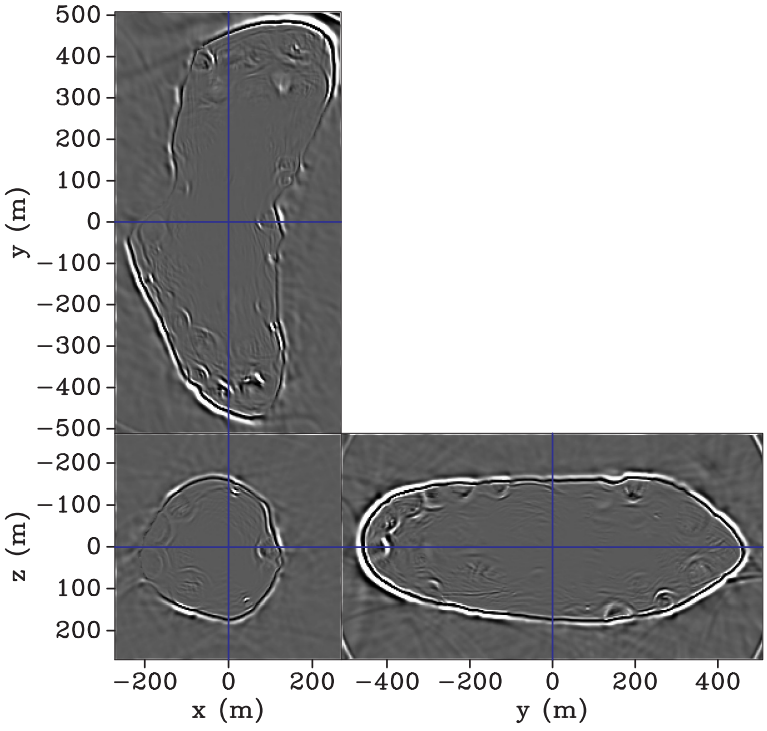

(b)

Figure 3.5: Migrated images (b) obtained for average velocity model (a)

CHAPTER 4

3D ACQUISITION DESIGN

As dicussed in the preceding chapters, I propose to use two satellites that move in different orbits to generate multi-offset data. Both transmitter and receiver satellites are equipped with radar antennas to propagate and receive the electromagnetic waves to and from the asteroid target. In this section, I design a realistic acquisition with dual orbiter satellites, analyze the limitation of the acquisition, and improve the coverage of the data to enhance the image resolution.

4.1 Navigation and data collection design

In Chapter 2, I introduce the geodesic dome concept to create an even distribution of receiver and source coordinates, and I use these coordinates to perform 3D imaging of the target. In this chapter, I explain how to use the geodesic dome as a tool to collect the source and receiver data when both spacecrafts orbit around the asteroid target. When the acquisition is complete, I can re-sort the multi-offset data (i.e. form a shot gather) so that one source location has its own set of receiver coordinates. The final shot-record migrated image is the stack of all the migrated images from different shots.

An asteroid tends to spin around its principal axis of rotation to maintain the lowest energy state (Pravec et al., 2002). The rate of rotation depends on the size, shape, and interior structure and composition of an asteroid. The graph in Figure 4.1 shows the normalized spinning rate (revolution/day) of small asteroids (0.15 km $<$ D $<$ 10 km). For realistic acquisition design, I configure the asteroid to rotate around its north pole (its principal axis) with a spinning period of 5 hours. My 3D acquisition design is based on a fixed reference frame (the asteroid is static relative to the source and receiver locations). Since an asteroid's rotational speed is faster than the speed of the revolving spacecraft, I cannot extract the

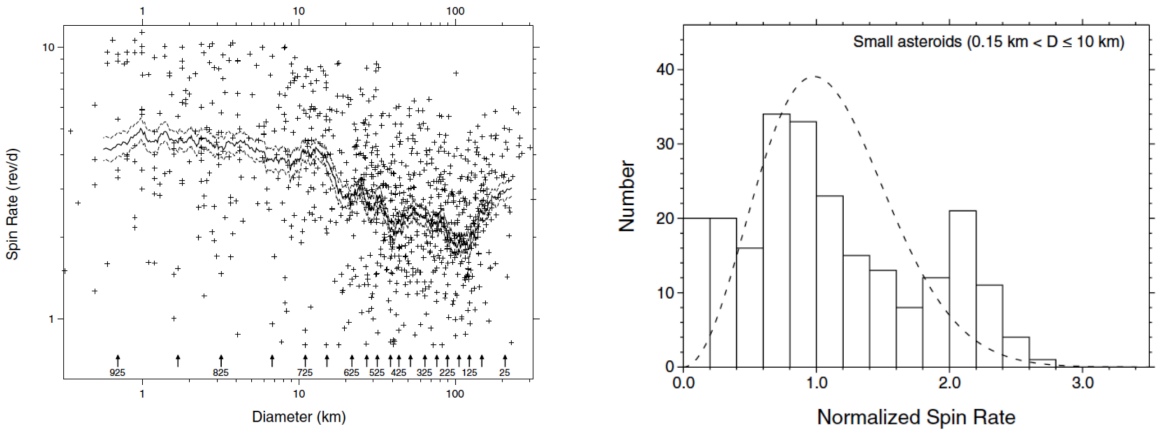

(a) (b)

Figure 4.1: Pravec et al. (2002) show results of an asteroid rotation rate study that includes (a) the relationship between the spinning rate distribution and the size of asteroids, (b) the normalization of the spinning rate of small asteroids (0.15 km $<$ D $<$ 10 km)

source and receiver coordinates using the navigation path of the spacecraft alone, but I must add the rotational period of the asteroid to the calculation.

For a fixed observer on a moving asteroid (which is our reference frame) during the time of acquisition, we can view the source and receiver satellites (targets) moving at the same revolving speed in the opposite direction of the spinning asteroid. Hence, from my reference frame, it appears that calculating the speed and direction at which a source and receiver satellite move involves combining the speed and direction of the source and receiver satellite and the speed of the asteroid rotation as shown in Figure 4.2. The geodesic dome is also generated within the same asteroid reference frame (i.e., the frame is static relative to the asteroid location). Using a given orientation and speed of an asteroid, I fix the geodesic dome (which is related to the asteroid coordinate) in space and adjust the orientation of the transmitter and receiver satellite orbits so that they rotate at the same relative speed as the asteroid. This enables one to plot a 2D-ground track map to show the extent of coverage made by the navigation path of the satellite. I record the positions of all the sources that lie within the equilateral triangles (from a given geodesic dome) and their corresponding

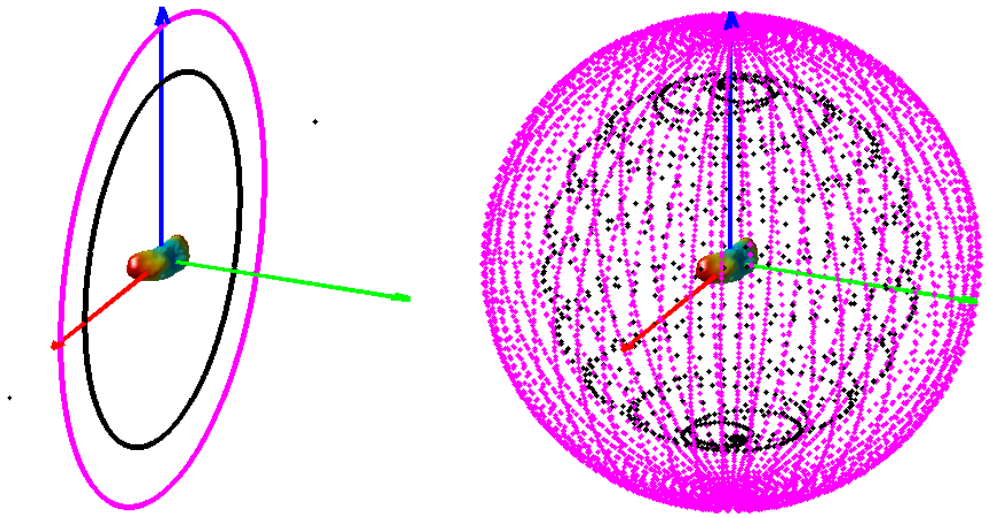

(a) (b)

Figure 4.2: (a) Design with the fixed orbit of the transmitter (in black) and receiver satellites (in pink) in the polar coordinate, (b) ground track representation (asteroid reference frame) with a constant spinning rate of an asteroid in the longitudinal direction

receiver locations to form shot-record data for the target source.

4.2 Realistic acquisition design

In one acquisition setup, the transmitter and receiver satellites rotate in the same latitudinal plane direction. The radius of the orbit determines the speed and revolving period of the satellite. The transmitter is located at a 1.9 km radius with a revolving period of 100 hours; the receiver is located at a 2.5 km radius with a revolving period of 151 hours. I assume that the shape and density of the asteroid and satellites have point-mass distribution and that they rotate with a perfectly circular motion, which follows Newtons third law. If the asteroid is fixed, I acquire shot-record data similar to a 2D acquisition and imaging design because the source and receiver orbits are limited to the same revolving plane. With the constant spinning rate of an asteroid in the longitudinal direction, I am able to perform 3D imaging using the additional illumination from the spinning asteroid target. From the asteroid reference frame, both satellites rotate at a speed that includes the additional longi-

tudinal speed resulting from the spinning asteroid. In general, the rate at which the asteroid spins is faster than the rate at which the transmitter and receiver rotate, and this creates the spiral navigation path of the satellite from the fixed asteroid reference frame. At each source location, I record the corresponding receiver locations and use these coordinates to perform shot-record imaging. The distribution of receivers for each source varies depending on the location of the source. The closer the source to the pole, the more receiver coverage one gets. When the asteroid rotates only in the longitudinal direction, the shot-record data distribution does not cover the entire spherical surface because both the source and the receiver are in the same longitudinal plane, which limits data aperture. In other words, the receiver coordinates are located only within the same longitudinal coordinates as the source. Thus, when the source and receiver rotate within the same longitudinal orbit, one obtains only limited aperture due to the size of the source patch.

If one uses a design where the source and receiver rotate within the same latitudinal orbit and the asteroid rotates in the longitudinal direction, the time of acquisition can be calculated using the least common multiple of 3 independent orbiting periods: that of the transmitter, receiver, and the asteroid target. This acquisition time represents the time needed for the satellite to fly back to the same location and begin repeating the same navigation paths.

The limited shot-record data aperture (due to the limited area of the triangular patch in the source geodesic dome) is shown in Figure 4.3 (at the equator) and Figure 4.4 (at the pole). Here, I experiment with increasing the time of acquisition from 1,200 hours to 6,000 hours and observe the density pattern of the shot-record data coverage. The longer the acquisition time, the more receivers one gets, but the receiver coordinates exist only in the limited-aperture area shown in Figure 4.5 (a) and (b). I also increase the radius of the receiver satellite from 2.5 km to 3.1 km, which eventually increases the revolving period of the receiver orbit. This results in better coverage in terms of radius, but the shot-record receiver coordinates are limited to the area of the source triangular patch shown in Figure 4.5 (b) and (c).

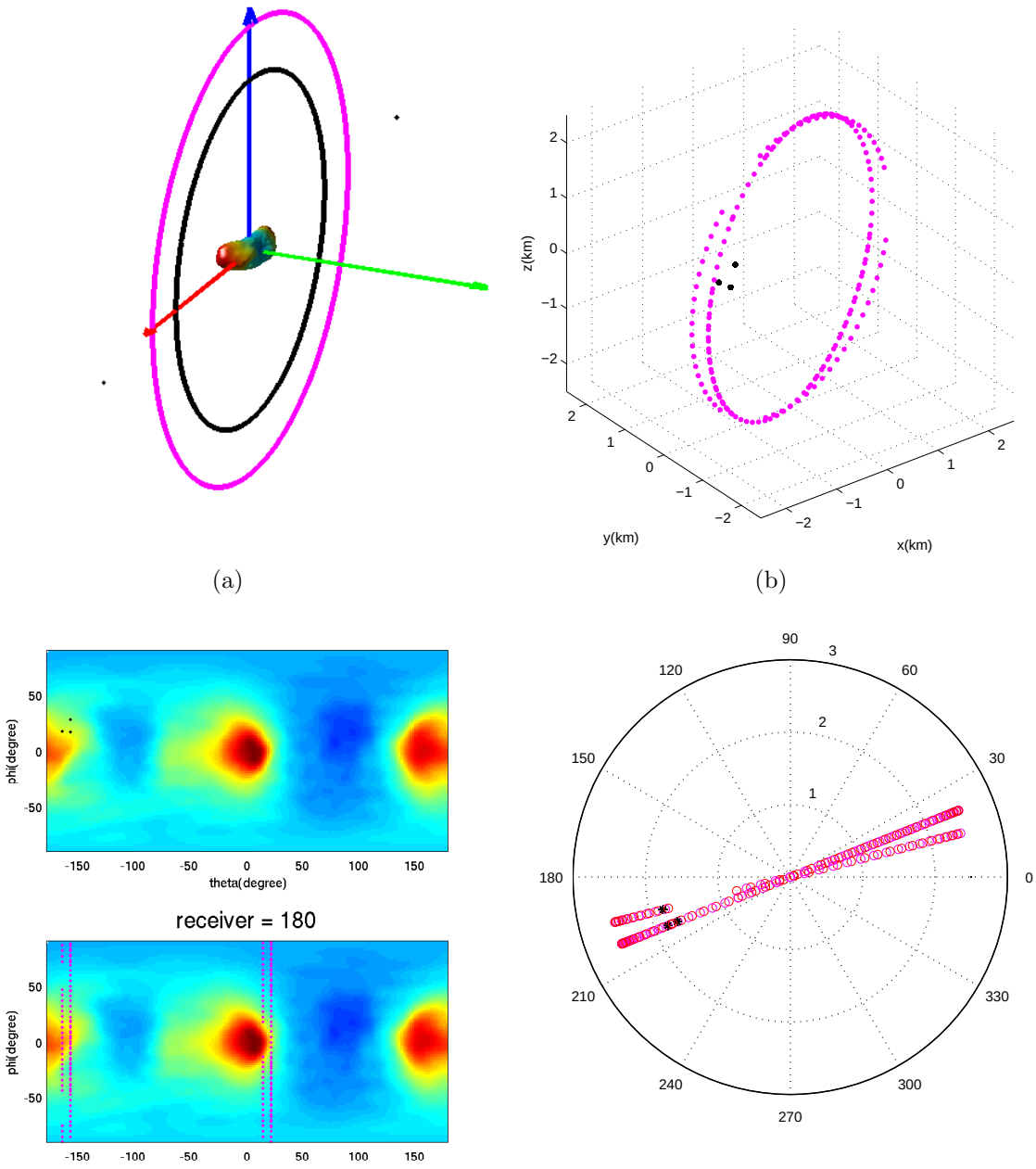

(a) (b) (c) (d)

Figure 4.3: (a) Design with transmitter and receiver satellites in polar orbit with 6,000 hours of acquisition time, (b) shot location at an equator triangular patch with black dots representing shot and pink dots representing receivers, (c) ground track map of the receiver and source location, (d) the top-view (polar) of the source-receiver distribution.

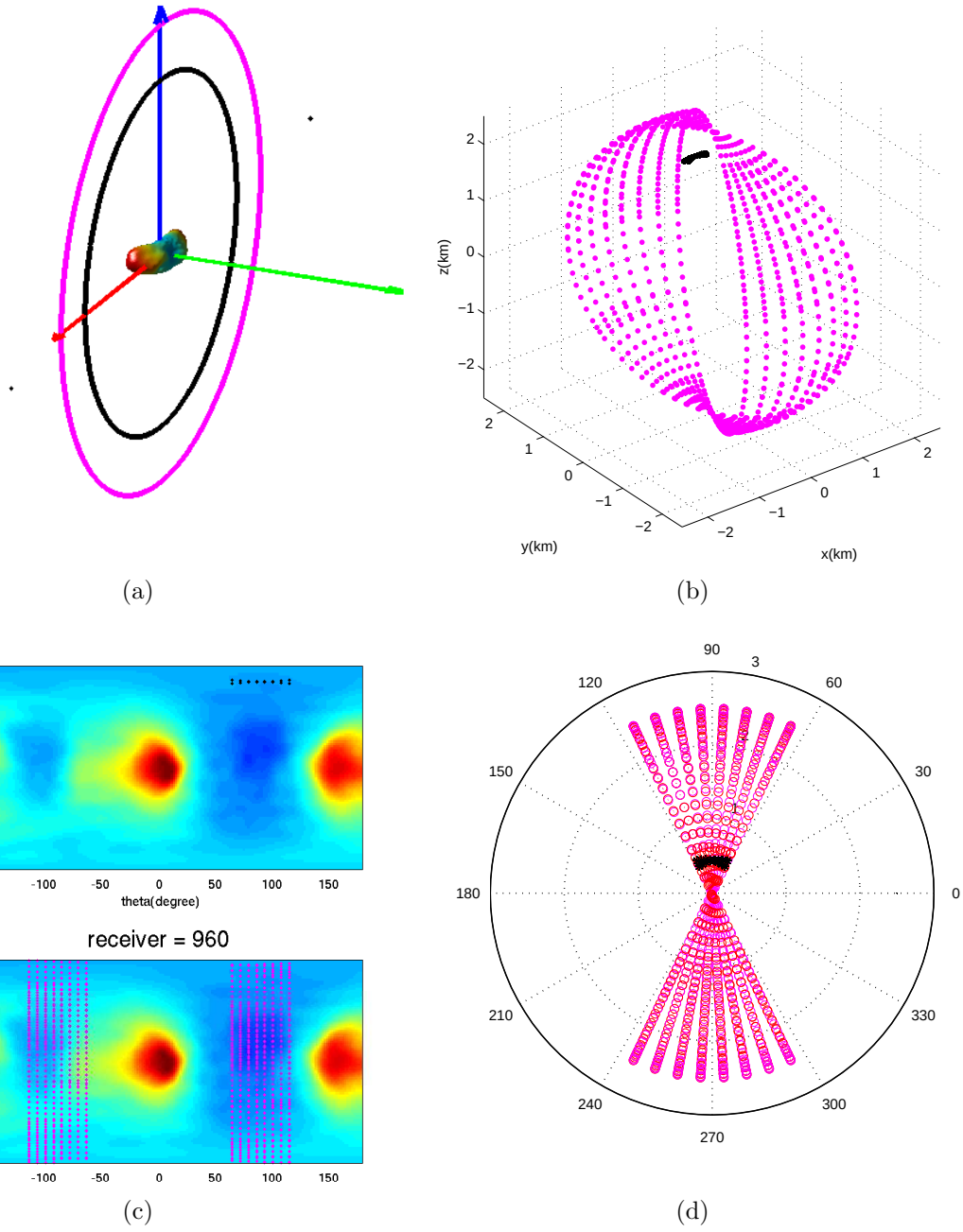

(a) (b) (c) (d)

Figure 4.4: Panels (a)-(d) are the same as in Figure 4.3 except for the shot location is located in the pole, instead of the equator.

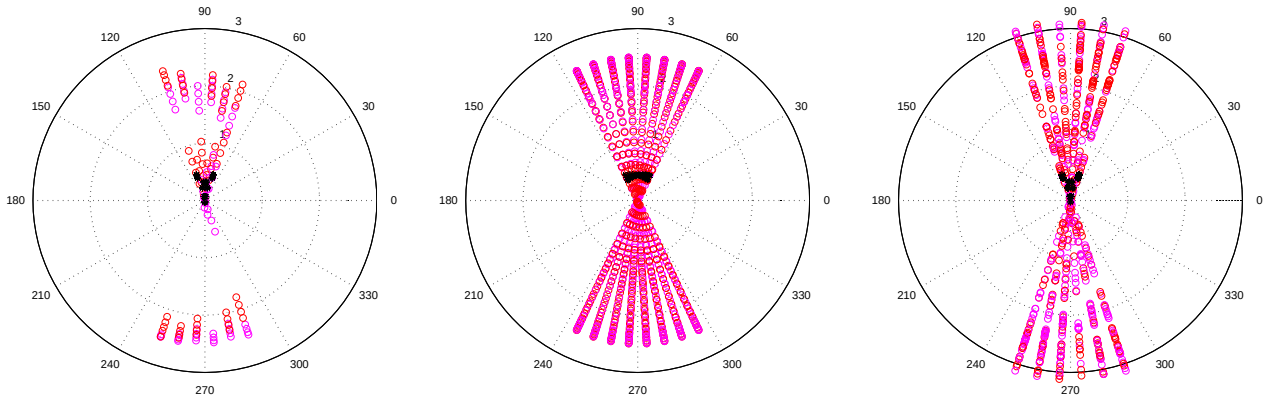

(a) (b) (c)

Figure 4.5: Acquisition design with the fixed orbit of the transmitter and receiver satellites in the polar orbit: shot-record receiver coverage at (a) 1,200 hours of acquisition time, (b) 6,000 hours. Acquisition design with (c) receiver satellite radius increasing from 2.5 km to 3.1 km (with decreasing orbital speed) shows shot-record receiver coverage at 6,000 hours

For a longitudinally rotating asteroid, dual coplanar orbiter systems are not sufficient to image the entire target due to the limited receiver coverage in the shot-record domain. Shot-record receiver coverage (even the shot located at the pole shown in Figure 4.4) from the coplanar orbiter systems is limited to the location and the area that the transmitter satellite covers as shown in Figure 4.3. In order to acquire full coverage of the receiver coordinates for each source, at least one orbital plane has to move around the asteroid target.

4.3 Alternative acquisition designs

To get better receiver-coordinate coverage in a shot-record experiment, I can alter the source and receiver longitudinal offset and shift the inclinational angle of the receiver orbit (relative to the angle of the source orbit) to create complete acquisition around the asteroid target. I show 6 different designs (Figure 4.6) that improve the shot-record data coverage. In Design 1, the source orbit is fixed at 0 degrees in longitude and the source rotates only in the latitudinal direction; the receiver orbits shift 36 degrees in the longitudinal direction every 500 hours. After 6,000 hours, I get full coverage of shot-record data around the

asteroid. Design 2 has the same setup as Design 1, except that the receiver orbit rotates in the inclinational (latitudinal) direction. In Design 3, both source and receiver orbits rotate at different speeds in the opposite longitudinal direction. In Design 4, I alter both source and receiver orbits in the inclinational direction. In Design 5, I alter the source orbit in the inclinational direction and shift the receiver orbit in the longitudinal direction. The only difference between Design 5 and Design 6 is that the source rotates in the longitudinal direction while the receiver rotates in the latitudinal direction. Designs 1-6 are also listed in Table 4.1, where T represents transmitter satellite orbit and R represents receiver satellite orbit. With these designs, I can generate better coverage of the shot-record data within a given acquisition time.

Because the velocity changes for shifting the satellite orbits in the longitudinal and inclinational directions are equal, the energy used is relatively the same for both directions (Prussing et al., 1993). The coverage and distribution of the receivers for each shot record migration is shown in the imaging section. After the shot-record data are acquired within a limited acquisition time, I use the source geodesic dome to rearrange and record the data in the imaging step. I run migration from partial sources (selected from the geodesic dome distribution) in the survey. To get the final 3D image, I stack all experimental images from the selected partial sources.

Inclinational and longitudinal orbital shift mechanics

Near-Earth object (NEO) exploration is a feasible mission due to the low propulsive change in velocity and a short time of acquisition (less than a year) (Augustine et al., 2009). Acquisition cost (a critical element for making a launching decision) depends on the energy used in maneuvering the spacecraft orbit, and this cost directly depends on the change in velocity value. The velocity change is a scalar quantity that explains the change in spacecraft velocity required by the propulsive system during the mission (Prussing et al., 1993). The maneuver requires the velocity change to be orthongonal to the orbital plane. If the shifted orbital plane remains the same size as the initial plane, the required change in velocity

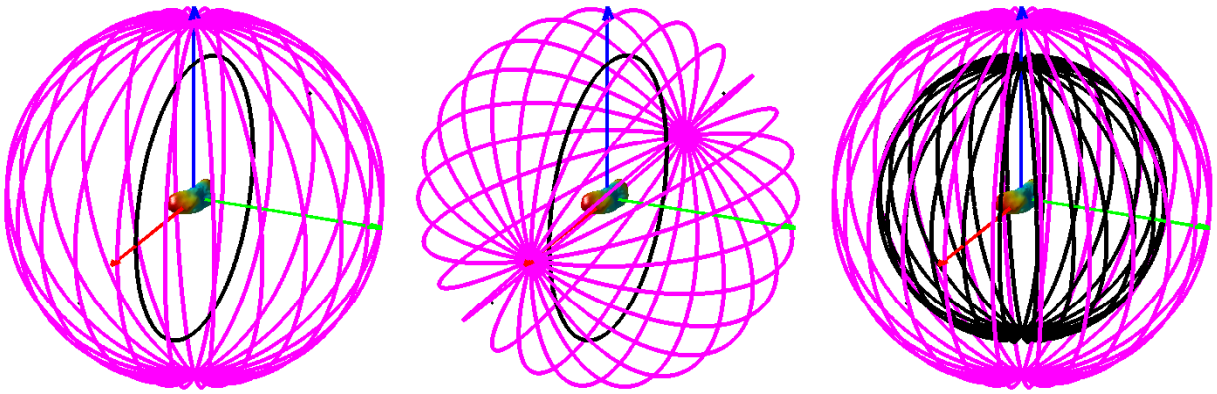

(a) Design 1 (b) Design 2 (c) Design 3

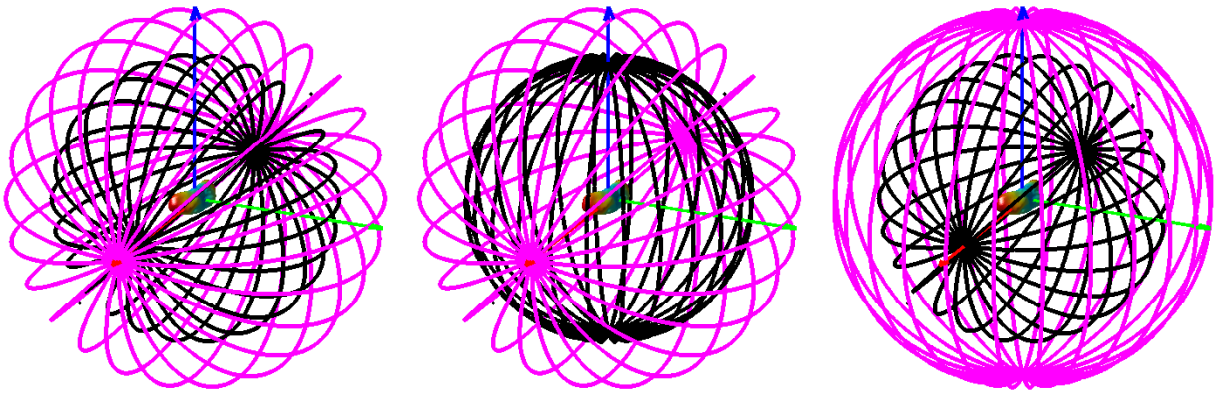

(d) Design 4 (e) Design 5 (f) Design 6

Figure 4.6: 3D acquisition designs. For the acquisition time of 6,000 hours, I design 6 possible navigation paths for dual orbiter acquisition. The details (a)-(h) of the acquisition designs are included in Figures 4.7-4.12.

formulation is simplified to

$$\Delta V = 2V_i sin\left(\frac{\theta}{2}\right), \tag{4.1}$$

where V_i is the initial velocity of the plane and θ is the angle of orbital shifts (Prussing et al., 1993). Since, NEOs have a low δv (< 4.5 km/s) on average (Elvis et al., 2011), the additional fuel needed to change the orbital plane is minimized. The six alternative 3D acquisition designs presented in this thesis are possible in terms of the minimal additional cost and the mechanics of shifting an orbital plane. The mechanics of performing this shift involves burning fuel around the intersection points (orbital nodes) of the two orbital planes. The cost of changing the orbital plane both in the inclinational and longitudinal directions is the same.

As the coplannar orbiter systems fail to achieve full receiver coverage and at least one orbital plane shift is required, the cost of changing the orientation of the satellite's orbital plane should be considered when choosing an acquisiton design. I select the best design from

Table 4.1: Acquisition Designs

Options	Design 1	Design 2	Design 3	Design 4	Design 5	Design 6
Polar orbit	T	T				
Longitudinal shift	R		T and R		T	R
Inclinational shift		R		T and R	R	T

the above 6 choices by observing the distribution of receiver locations in the shot-record domain, which is shown in Figure 4.7-4.13 (b) and (d). Each design acquires data within the same time of acquisition. The more evenly distributed the receiver locations on the geodesic dome, the better the imaging quality (i.e., the higher the signal-to-noise ratio). I use two analyses to find the best acquisition design. In the first analyss, I discretize the 2D ground track map (Figure 4.7-4.13 (c)) (showing receiver navigation paths) into rectangular grids and apply the weighting function, $cos(\phi)$, at each binning area, where ϕ is the latitudinal information from the receiver. I record the receiver navigation paths on the geodesic dome

and apply the mean square deviation to each triangular patch on the dome. I then implement the information gathered from the two analyses for all design experiments (1-6) and select the design that has the lowest value of mean-square deviation:

$$R = \frac{\sum_{p} \left(\frac{d - d_{avg}}{d_{avg}} \right)^2}{N * (N-1)^2}, \tag{4.2}$$

where R is the minimization level, N is the number of patches (discretization grid cells), p is the number of the patch that represents the receiver discretization both in the rectangular grid and the geodesic dome, d is the number of receivers located in each patch, and d_{ave} is the average value of the total number of receivers in the domain divided by the number of patches. In the ideal case, the receiver coordinates are evenly distributed on the area, as given by $d = d_{ave}$ and $R = 0$. This calculation is the standard deviation of the number of receivers in a patch scaled by the worst receiver distribution case, where all receivers locate in only one patches. Hence, when $R = 1$, all receivers locate in one patch and when $R = 0$, the receiver coverage is evenly distributed in the sphere. The number of receivers accounts for differences in overall density due to the various geometries of the shot-record receivers within 60-degree reflection angle.

From the optimization analysis of all receivers (Figure 4.13), the receiver distribution depends only on the navigation path of the receiver satellite. Hence, Designs 1 (Figure 4.7), 3 (Figure 4.9), and 6 (Figure 4.12), where the receiver satellite rotates longitudinally, have identical distribution of receivers as opposed to Designs 2 (Figure 4.8), 4 (Figure 4.10), 5 (Figure 4.11), where the receiver orbits in the inclinational direction. The longitudinal orbital shift design repetitively accumulates a large number of receiver coordinates at the north and south poles in contrast to the inclinational orbital shift design, which has a high accumulation of receiver coordinates at each equator location (nodal points). By observing the receiver distribution, I can determine whether to leave one or both spacecraft in polar orbit. The source-receiver coverage can be visualized from the shot-record midpoint coverage

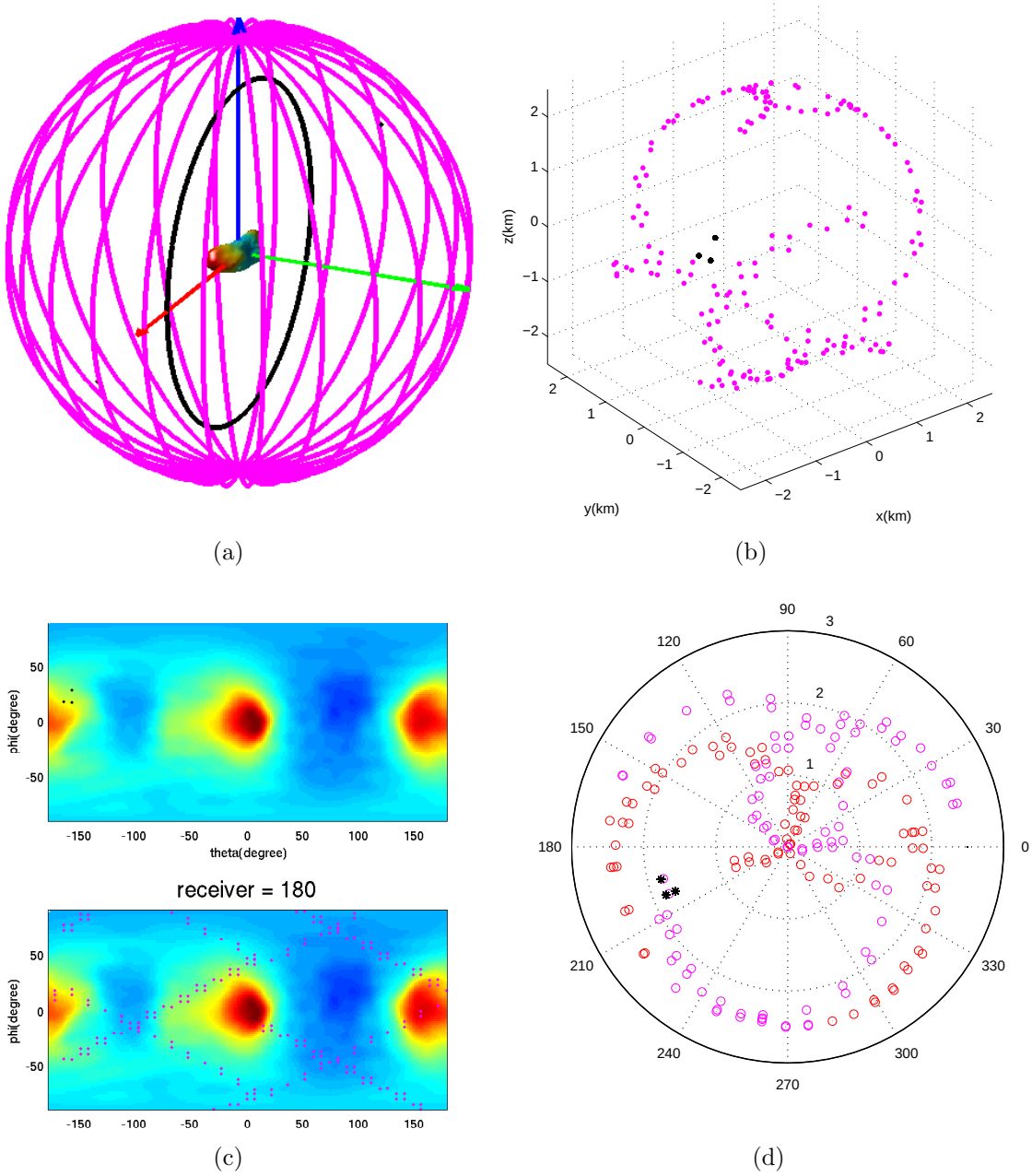

(a) (b) (c) (d)

Figure 4.7: Design 1. With the fixed orbit of the transmitter satellite, the receiver satellite rotates in the latitudinal direction and alters its orbit in the longitudinal direction. (a) 3D orientation of shifted plane (b) shot location at the equator triangular patch with black dots representing shot and pink dots representing receivers, (c) ground track map of the receiver and source location, (d) the top-view (polar) of the source-receiver distribution.

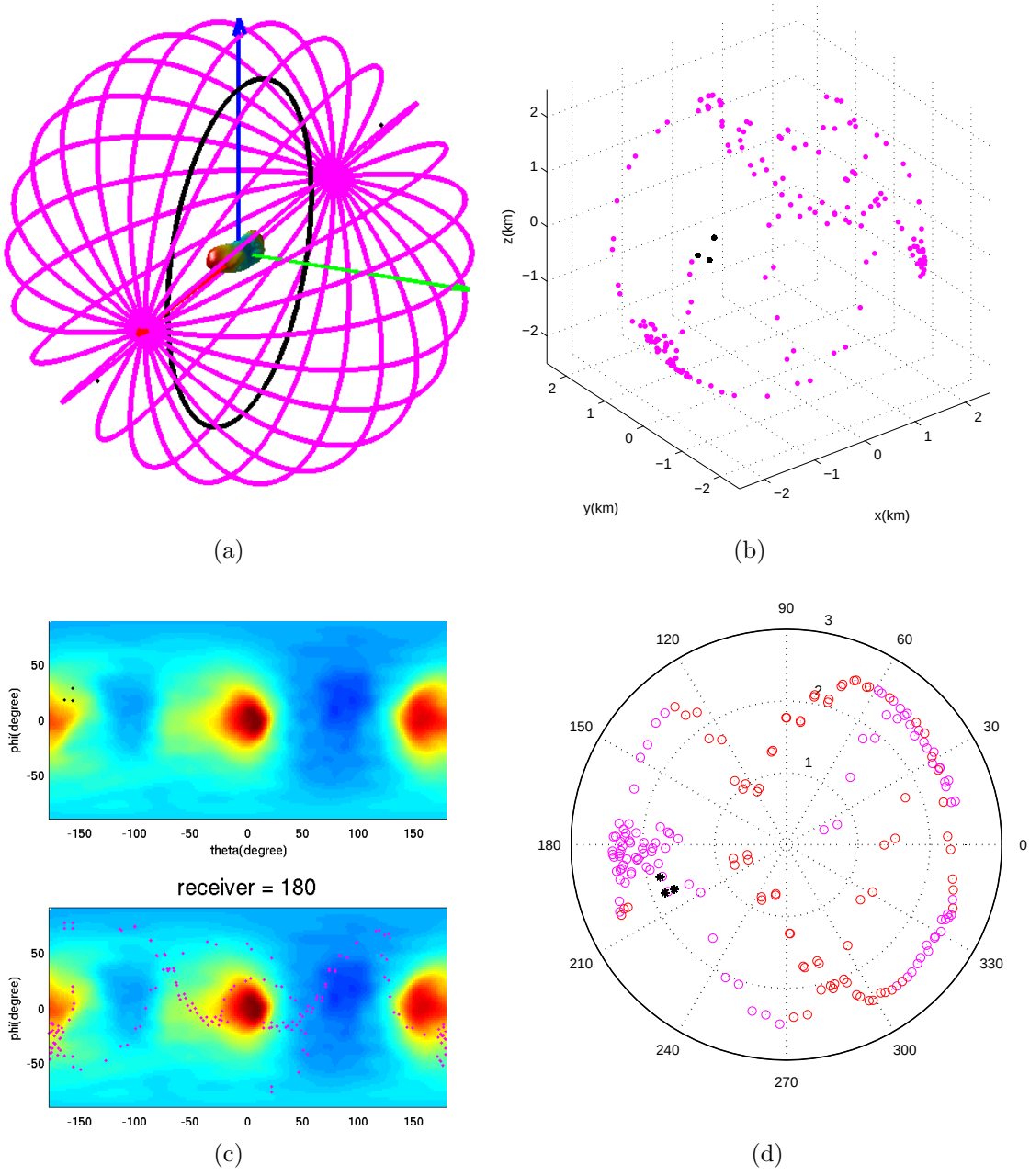

Figure 4.8: Design 2. The receiver satellite alters its orbit in the inclinational (latitudinal) direction with the fixed orbit of the transmitter satellite. Panels (a)-(d) are the same as in the Design 1.

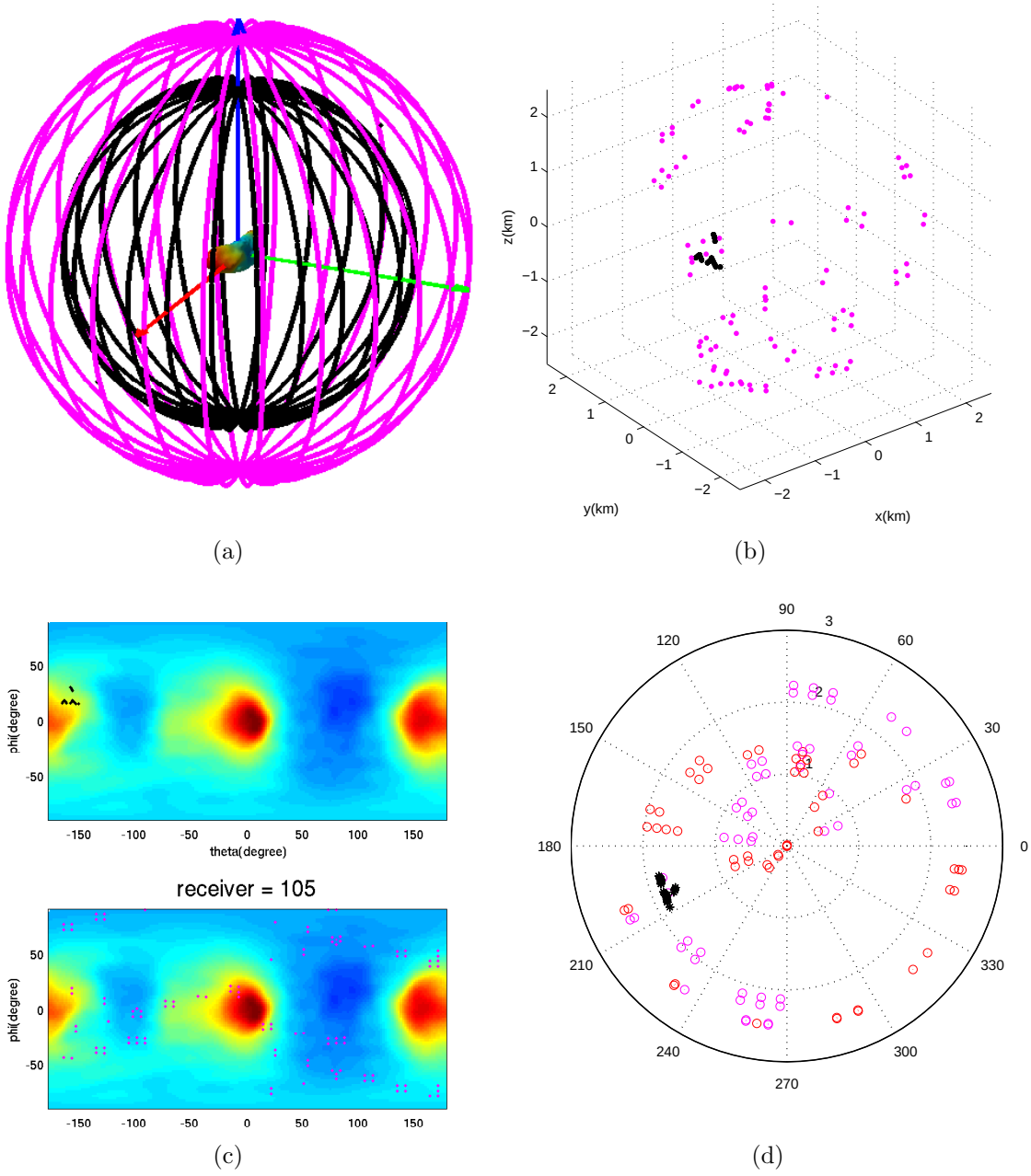

(a) (b) (c) (d)

Figure 4.9: Design 3. Both the orbits of the receiver and transmitter satellites shift in the longitudinal direction at different revolving rates and directions. Panels (a)-(d) are the same as in the Design 1.

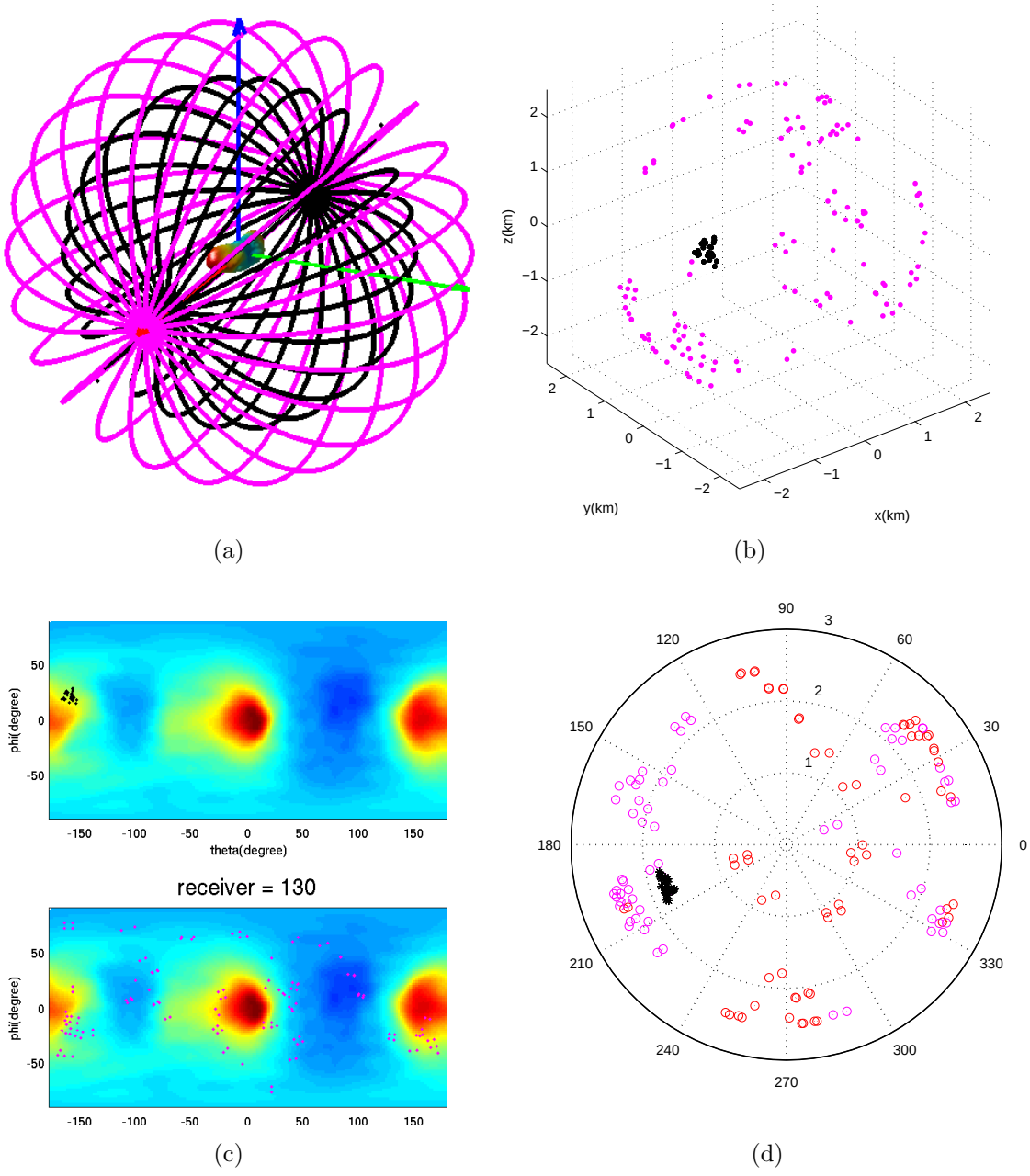

(a) (b)

(c) (d)

Figure 4.10: Design 4. Both receiver and transmitter satellites rotate in the latitudinal direction with different rates and directions of rotation. Panels (a)-(d) are the same as in the Design 1.

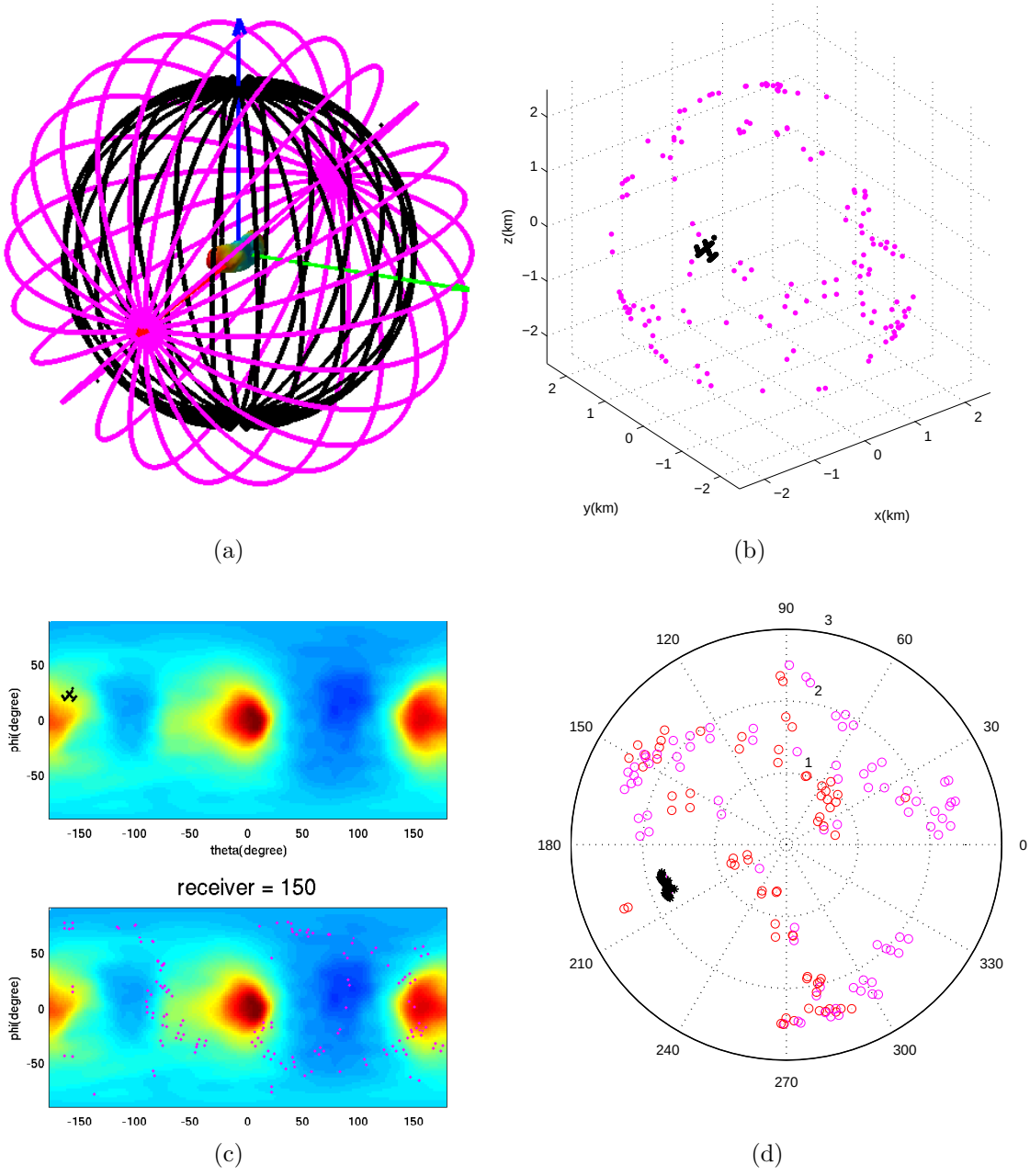

(a) (b)

(c) (d)

Figure 4.11: Design 5. The orbit of the receiver satellite shifts in the longitudinal direction and the transmitter shifts in the latitudinal direction. Panels (a)-(d) are the same as in the Design 1.

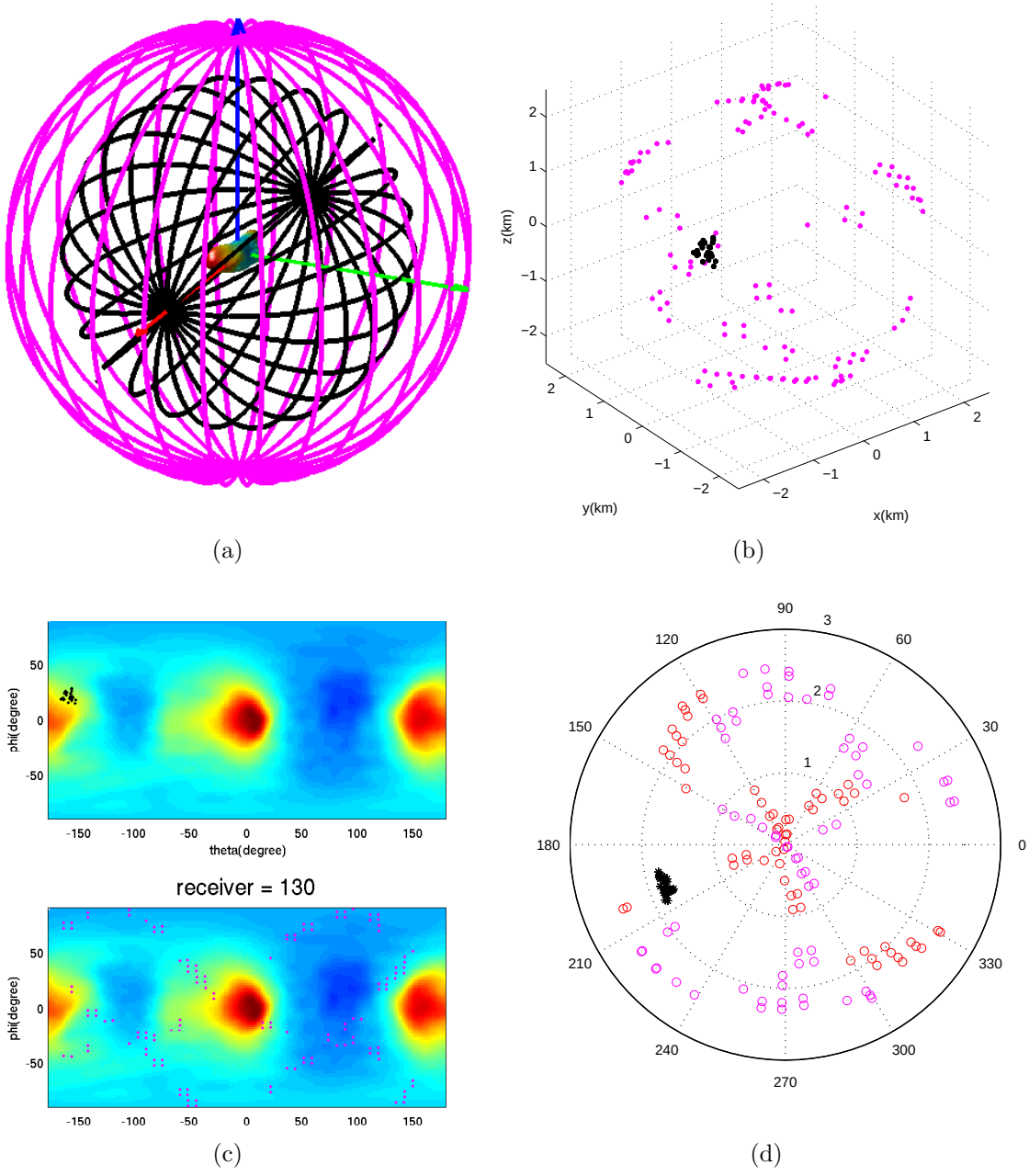

(a) (b)

(c) (d)

Figure 4.12: Design 6. The transmitter satellite shifts in the longitudinal direction and the receiver satellite shifts in the latitudinal direction. Panels (a)-(d) are the same as in the Design 1.

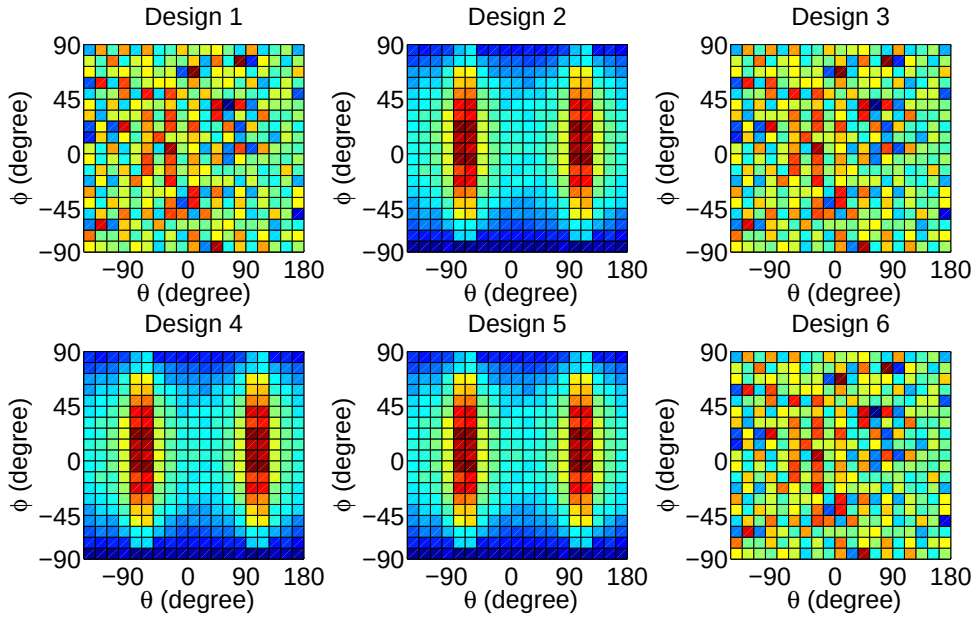

(a)

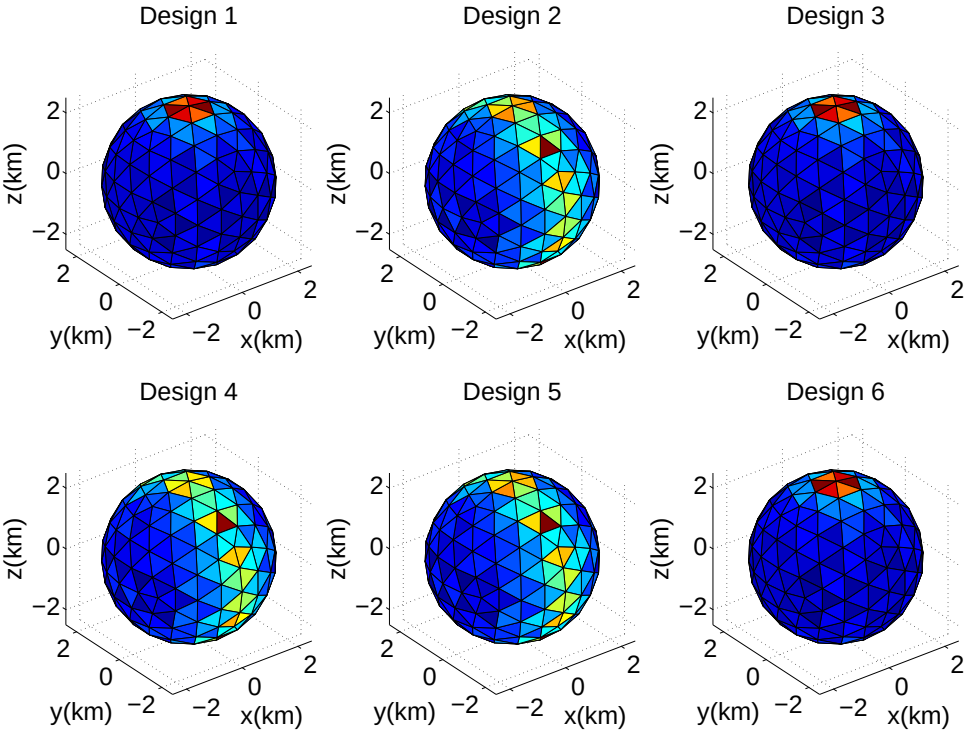

(b)

Figure 4.13: Analysis of receiver coordinate coverage for the six acquisition designs (not limited to source location and aperture): (a) rectangular grid representation, where ϕ is the latitude and θ is the longitude in the ground track map, (b) geodesic dome representation.

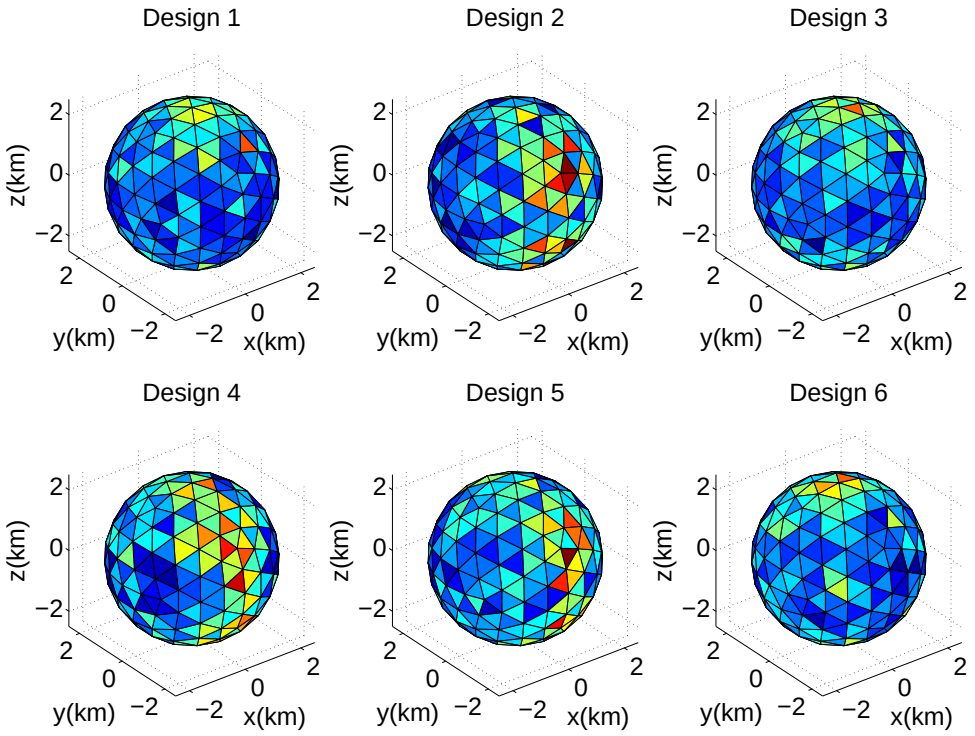

(a)

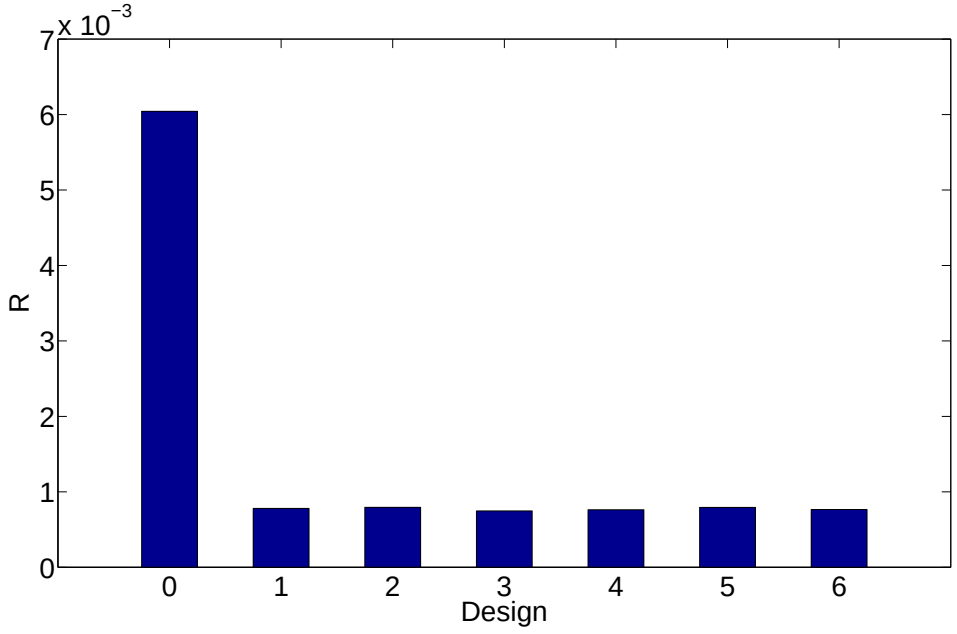

(b)

Figure 4.14: 80 shot-record receiver coverage: (a) geodesic dome optimized representation, (b) minimization result on the geodesic dome

.

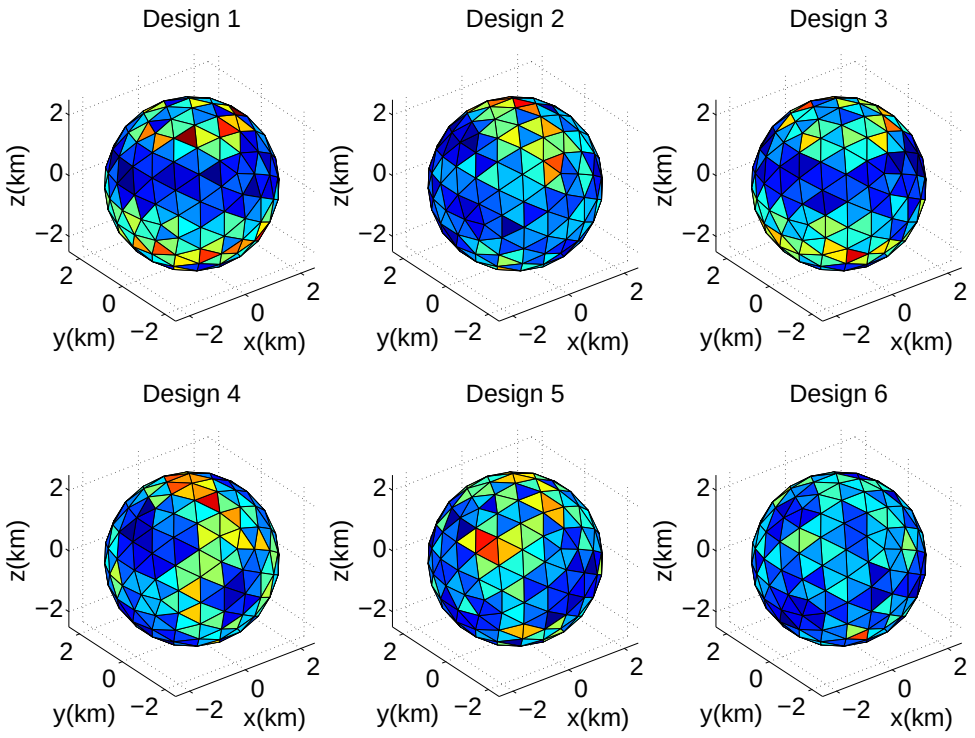

(a)

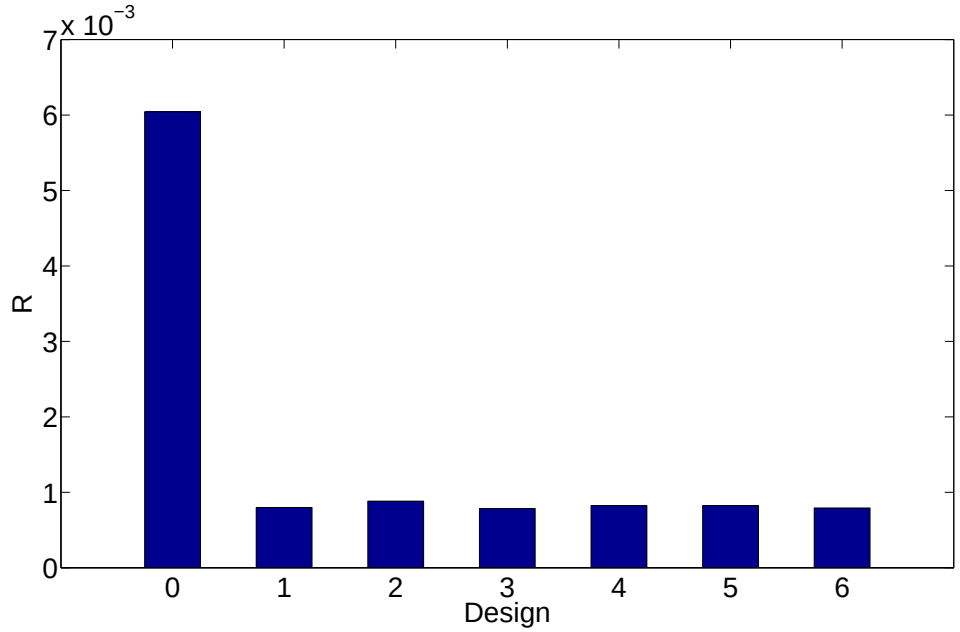

(b)

Figure 4.15: 80 shot-record midpoint coverage (fold map): (a) geodesic dome optimized representation, (b) minimization result on the geodesic dome

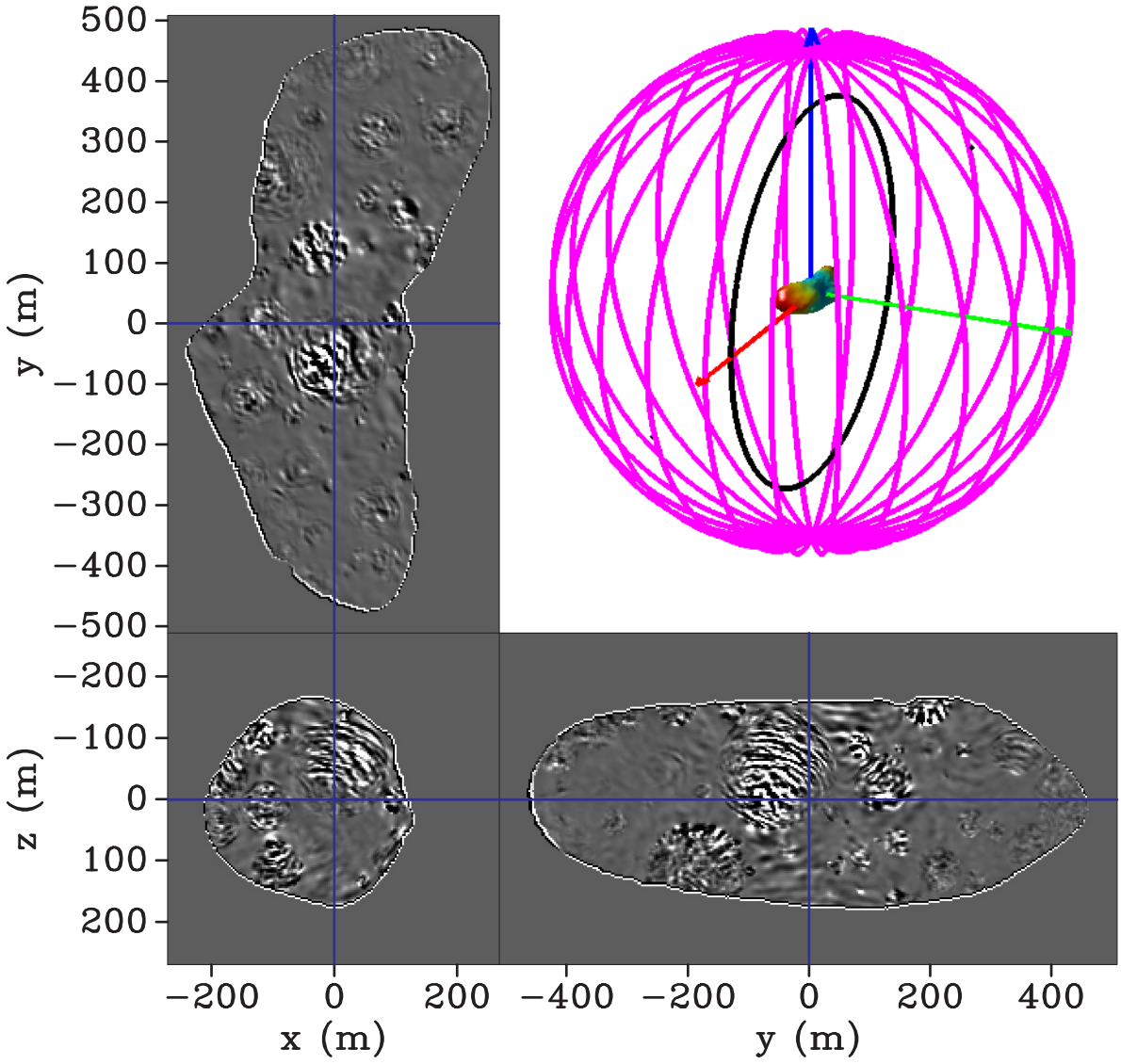

(a)

Figure 4.16: Corresponding migrated images (10 shot) obtained by wavefield-based migration using realistic acquisition (a) Design 1

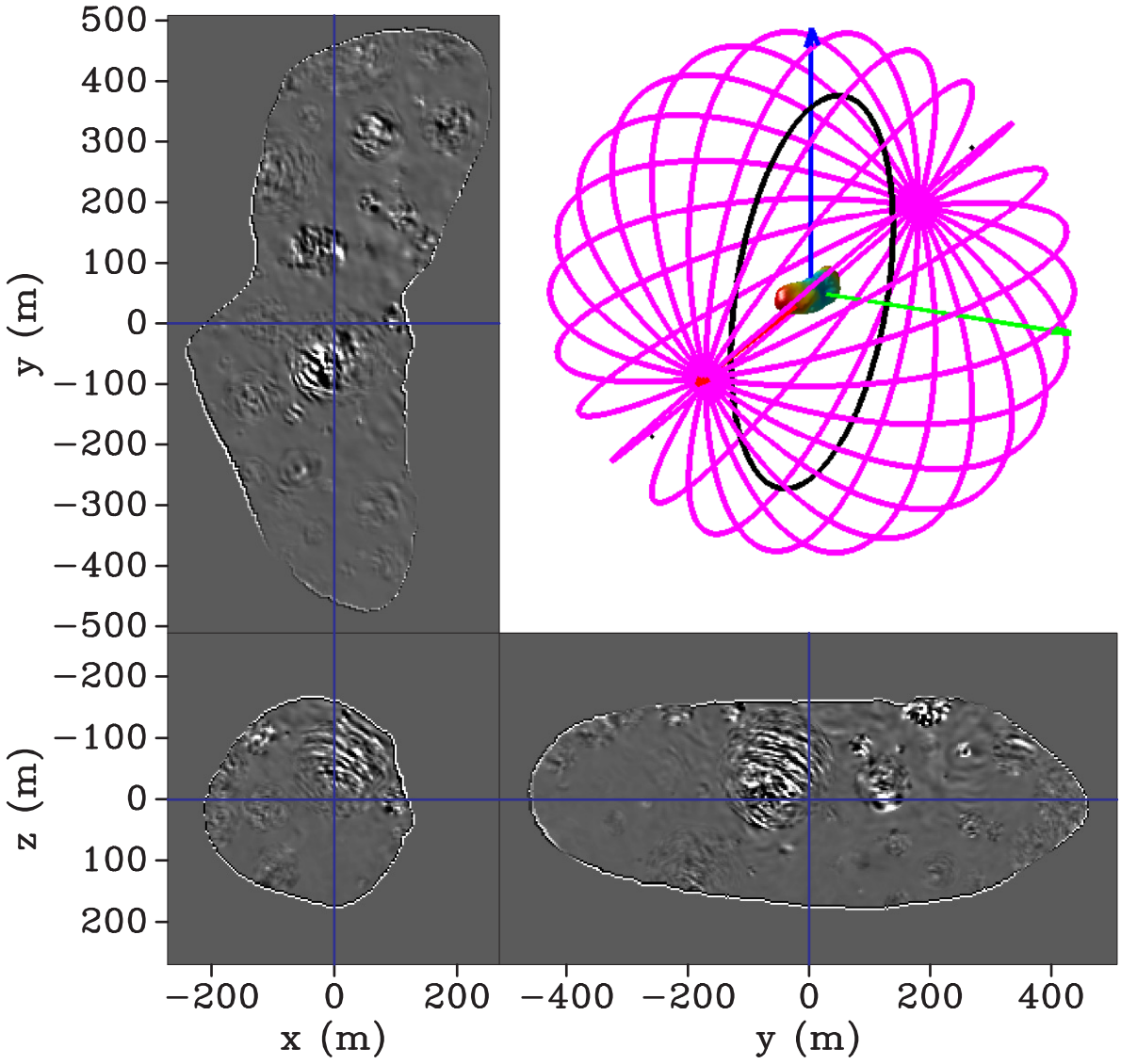

(a)

Figure 4.17: Corresponding migrated images (1 shot) obtained by wavefield-based migration using realistic acquisition (a) Design 2

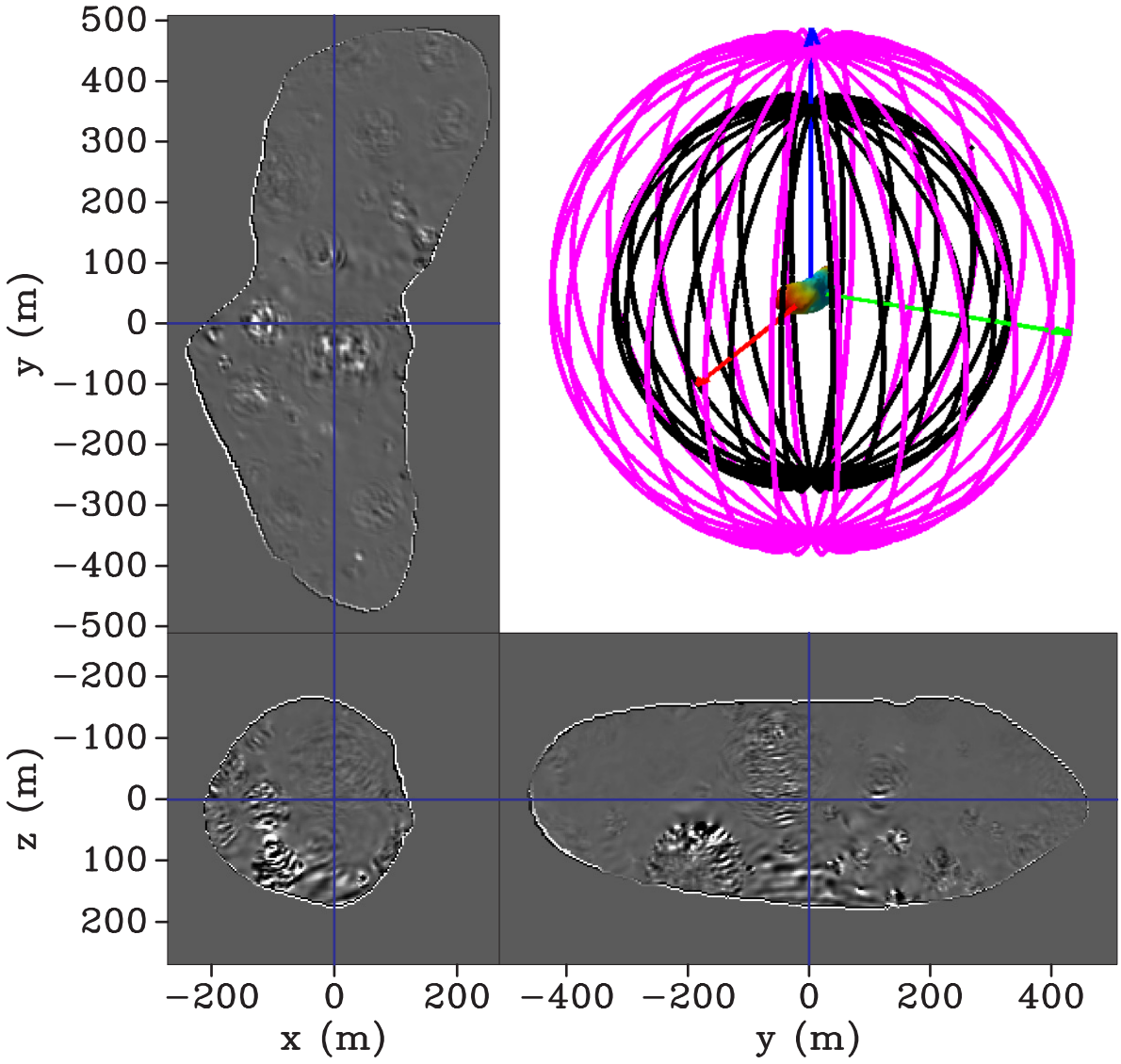

(a)

Figure 4.18: Corresponding migrated images (1 shot) obtained by wavefield-based migration using realistic acquisition (a) Design 3

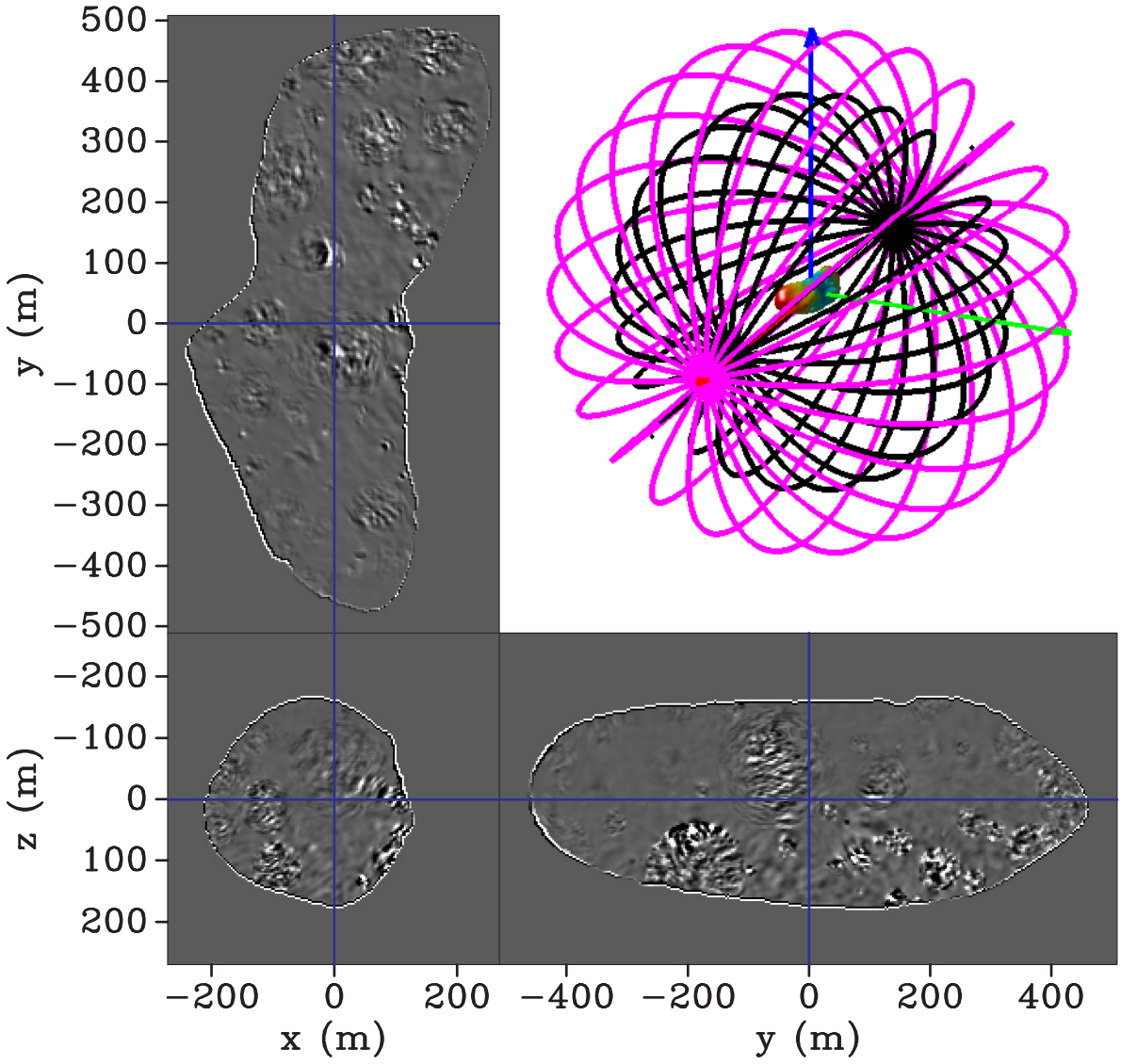

(a)

Figure 4.19: Corresponding migrated images (1 shot) obtained by wavefield-based migration using realistic acquisition (a) Design 4

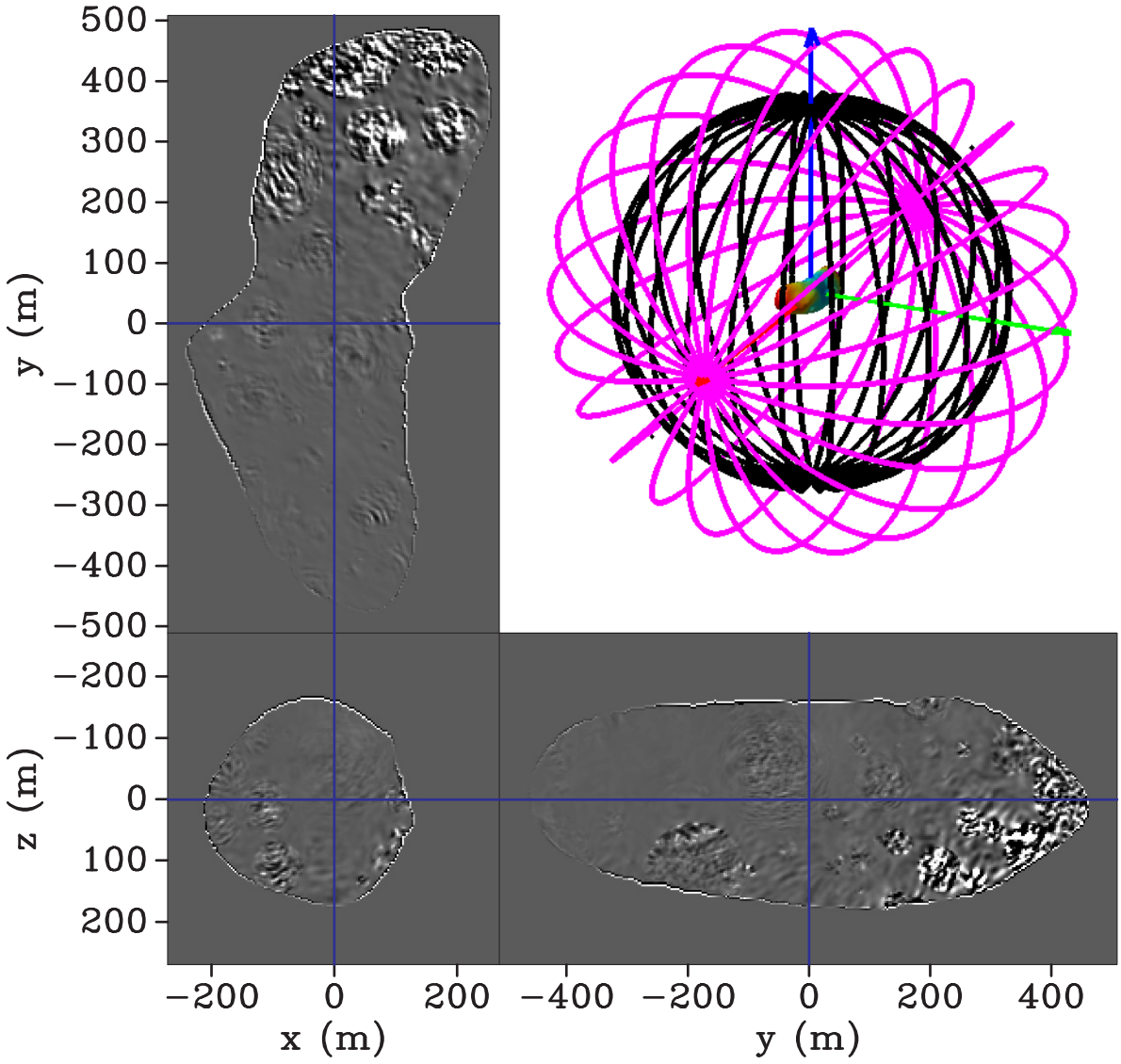

(a)

Figure 4.20: Corresponding migrated images (1 shot) obtained by wavefield-based migration using realistic acquisition (a) Design 5

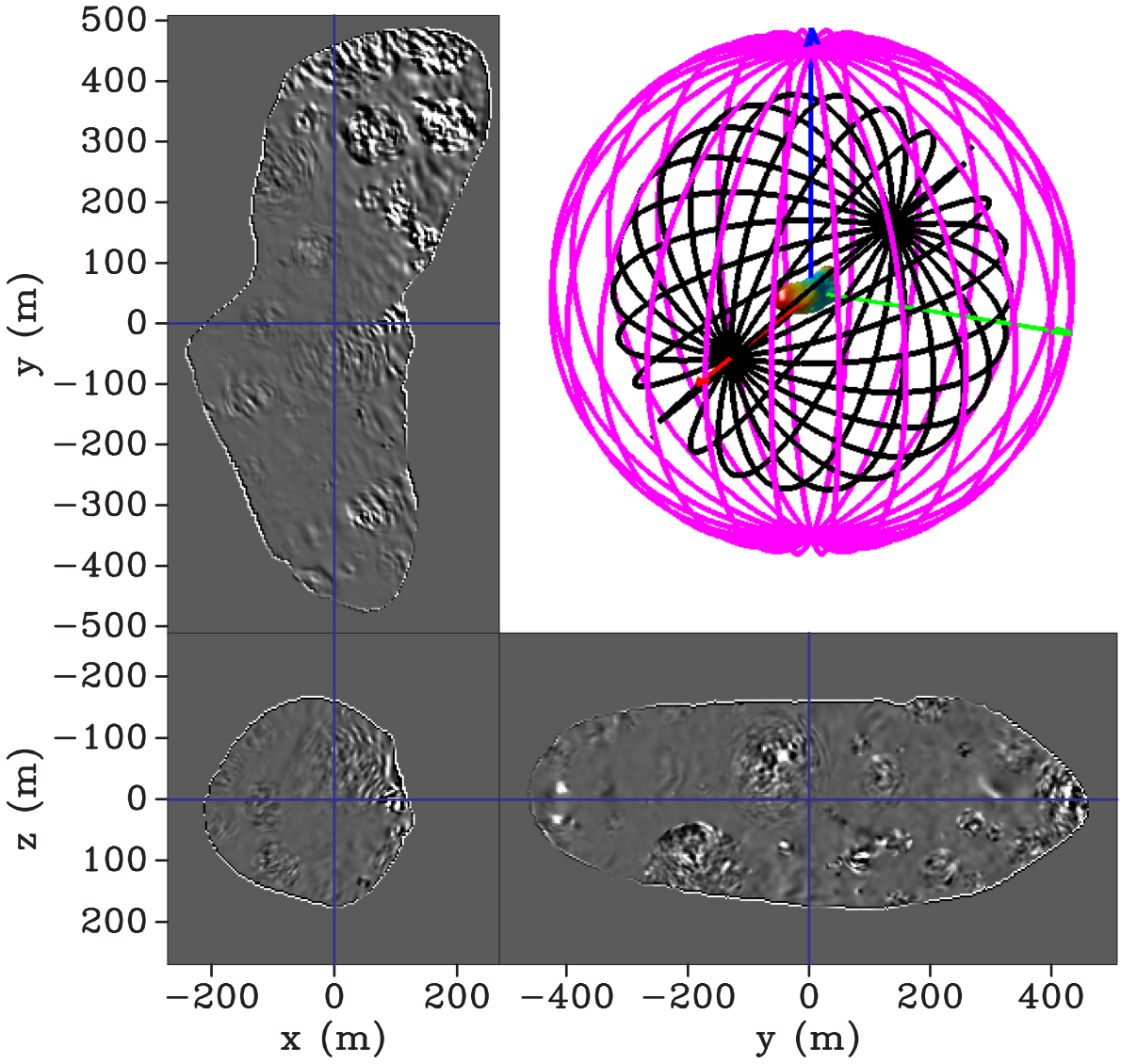

(a)

Figure 4.21: Corresponding migrated images (1 shot) obtained by wavefield-based migration using realistic acquisition (a) Design 6

(fold map) (Figure 4.15 (a)), where the midpoint represents the illumination location on an asteroid surface and is generated by calculating the midpoint between source and receiver coordinates relative to the asteroid reference frame. This coverage also shows the distribution of reflection points on the asteroid target generated from different acquisition designs. The minimization level is shown in Figure 4.15 (b), where Design 0 is represented the R-value of the coplanar design, and the Designs 1-6 are shown corresponding to Figure 4.15 (a). One can easily alter the orbit of the satellites in Designs 1 and 3, and both designs have identical receiver coverage due to the common receiver navigational paths. In order to choose between these two designs, one must consider the shot-by-shot receiver coverage. Analysis of this coverage (Figure 4.14) using 80 shots shows that all 6 acquisition designs provide similar coverage for receiver coordinates and all 6 designs create higher receiver distribution than Design 0, which is referred to the coplanar design, in the shot-record domain. Because the data accumulate over the pole for Designs 1, 3, 6 and at the nodal points for Designs 2, 4, 5, I reject bins (triangular patches) that have very high counts (where orbits intersect) to avoid biasing the distribution analysis results. I select 12 triangles with the highest counts and subtract these counts from the analysis. Without this bias, the standard deviations provide a result that reasonably represents the distributions of the receivers. There are different ways to shift the transmitter and receiver satellite orbits, and each acquisition design offers varied receiver coverage for shot-record imaging. The image quality improvement (due to higher coverage and the number of shot-record receivers) is not significant when one compares the migrated image quality of Design 1-6 as shown in Figure 4.16 - Figure 4.21. The acquisition cost is also much higher for Design 3-6 and therefore should be a crucial factor in the decision-making process for launching a space exploration program.

Designs 1, 3, and 6 have an inner satellite (receiver) that precesses in the the longitudinal direction(longitude of the ascending node), while the satellite in Design 2, 4, and 5 precess in the inclinational direction. Design 3-6 use an equal amount of energy because they apply the same δv at the same angles to the orbit direction. Thus, the cost of shifting only the

receiver satellite orbit for Designs 1 and 2 is less than the cost of shifting both the transmitter and receiver satellite orbits (which need to change their orbits concurrently) for Designs 3-6. The cost of shifting a spacecraft orbit in the longitudinal or inclinational direction is approximately the same. Hence, the cost of Designs 3-6 is double the cost of Design 1 and 2. However, one spacecraft in Design 2, 5, 6 must moved 90 degrees before starting to create a useful coverage map for 3D imaging. Thus, Design 1 is the most efficient solution both in regard to acquisition cost and image quality.

CHAPTER 5
DISCUSSION AND CONCLUSION

Following are some concluding remarks about the realistic 3D-imaging and acquisition design for asteroid exploration:

- The depth of penetration depends on the attenuation controlled by the asteroid conductivity. With high attenuation, the propagating electromagnetic wave gets attenuated and disappears before reaching the receiver coordinates at the other side of the target and therefore, no transmission data exist. The degree of attenuation also depends on the distance the wave travels inside the attenuated medium.

- 3D data coverage (for a single-shot location) is determined by the time of acquisition, the rotational velocity of both transmitter and receiver satellites, the spinning rate of an asteroid, and the size of the triangular patch considered on the source geodesic dome. As a result, realistic 3D asteroid acquisitions generate non-perfect (not dense and not uniform) data coverage on the spherical surface, and this data creates imaging artifacts. Increasing the number of sources and the time of acquisition improve image quality.

- The signal-to-noise ratio of the migrated image for dual-orbiter acquisition depends on the density and distribution of the near-array receivers and the number of stacking shots. For the ideal acquisition design, the receiver locations are sampled every 188 square meters per receiver and $1.41 \text{x} 10^5$ square meters per source. When source and receiver discretization is optimal and evenly distributed, the noise from cross-talk artifacts is reduced. The resolution of the migrated image also depends on the frequency and the discretization of the model in the finite-difference scheme. The survey design uses medium-frequency wave propagation to maintain the resolution and to avoid an

aliasing problem caused by the high frequency bandwidth. I use the aperture to separate data for two different image-processing steps: migration (reflection imaging) and tomography (velocity analysis). Here, I focus on the migration step using the assigned velocity and electromagnetic model. The tradeoff between acquisition cost and image resolution is complicated and still needs to be explored in the future. Also, the grid discretization of the model directly determines the image quality of an asteroid, but at the same time, a denser grid increases the computational cost for image processing.

- With a spinning asteroid target in the polar orbit beneath the coplannar orbital satellites, the latitudinal and longitudinal receiver coverage eventually fills up the satellite ground track; however the individual shot-record receiver coverage is limited to the coplanar direction of source and receiver. The low-earth orbiting (LEO) asteroids naturally precess in the longitude direction due to the minimum torque that is created at the equatorial bulge.

- I select a 3D acquisition design that offers a high number distribution of receiver coordinates in the shot-record domain. The more evenly distributed the receiver locations on the geodesic dome, the better the imaging quality. Among the six options, Design I (i.e., where both receiver and transmitter satellites rotate in the same polar orbit with different rates of rotation) is the most effective acquisition design because it has the highest distribution and the best coverage of receiver coordinates per source location. The corresponding migrated image generated from Design I is geologically comparable to the migrated image generated from the ideal acquisition (which requires uniform and dense receiver coordinates).

Imaging the interior structure of comets and asteroids in 3D is attainable using dual orbiter acquisition systems. The ideal 3D acquisition design provides dense and evenly distributed receiver coordinates which allow us to accurately image the interior of an asteroid using reverse-time migration of electromagnetic wavefields. In an actual 3D acquisition de-

sign, the shot-record receiver coordinates are not evenly distributed and limit the migrated image quality. I conclude that Design 1, where the transmitter orbits in the polar coordinate and the receiver orbit shifts in the longitudinal direction, is the most efficient acquisition design. Even with the long acquisition time, the distribution of shot-record receivers is still sparse. However, 3D migrated images created from shot-record data of realistic 3D acquisition designs are reasonably accurate for interpreting the interior structure of an asteroid.

REFERENCES CITED

Annan, A., W. Wallerand, D. Strangway, R. Rossiter, J. Redman, and R. Watts, 1975, The electromagnetic response of a low-loss, 2-layer, dielectric earth for horizontal electric dipole excitation: Geophysics, **40**, 285–298.

Augustine, N., C. D. W. Austin, M. B. Bejmuk, C. Chyba, E. Crawley, M. J. Greason, and C. Kennel, 2009, Review of us human space flight plans committee: Seeking a Human Spaceflight Program Worthy of a Great Nation, NASA, Washington, DC.

Barriot, J., W. Kofman, A. Henrique, S. Leblanc, and A. Portal, 1999, A two dimensional simulation of the Consert experiment (radio tomography of comet Wirtane): Adv. Space Res., **24**, 1127–1138.

Benna, M., J. Barriot, W. Kofman, and Y. Barbin, 2004, Generation of 3-D synthetic data for the modeling of the CONSERT experiment (the radiotomography of comet 67P/ChuryumovGerasimenko): Antennas and Prop., **52**, 709–717.

Berkhout, J. A., 1984, Seismic migration: Imaging of acoustic energy by wave field extrapolation: Imaging of acoustic energy by wave field extrapolation: Elsevier.

Bottke, W., A. Cellino, P. Paolicchi, and R. Binzel, 2002, An overview of the asteroids: The Asteroids III perspective: Asteroids III, University of Arizona Press.

Carry, B., 2012, Density of asteroids: Planetary and Space Science, **73**, 98–118.

Chapman, C., 2004, The hazard of near-Earth asteroid impacts on Earth: Earth Planet. Sci. Lett., **222**, 1–15.

Claerbout, J., 1986, Imaging the earth's interior: Geophysical Journal of the Royal Astronomical Society, **86**, 217–217.

Durda, D. D., F. W. Bottke Jr., D. Nesvorn, L. B. Enke, J. W. Merline, E. Asphaug, and D. C. Richardson, 2007, Sizefrequency distributions of fragments from SPH/N-body simulations of asteroid impacts: Comparison with observed asteroid families: Icarus, **186**, 498–516.

Elvis, M., J. McDowell, A. J. Hoffman, and P. R. Binzel, 2011, Ultra-low delta-v objects and the human exploration of asteroids: Planetary and Space Science, **59**, 1408–1412.

Festou, M., H. Kellera, and H. Weaver, 2004, A Brief Cconceptual History of Cometary Science: Comets II, University of Arizona Press.

Fisher, E., A. G. McMechan, A. P. Annan, and W. S. Cosway, 1992, Examples of reverse-time migration of single-channel, ground-penetrating radar profiles: Geophysics, **57**, 577–586.

Fomel, S., P. Sava, I. Vlad, Y. Liu, and V. Bashkardin, 2013, Madagascar: open-source software project for multidimensional data analysis and reproducible computational experiments: Journal of Open Research Software, **1**, e8.

Gaskell, R., 2008, Eros shape model v1.0: `sbn.psi.edu/pds/resource/erosshape.html`, NASA Planetary Data System.

Grasmueck, M., 1996, 3-d ground-penetrating radar applied to fracture imaging in gneiss: Geophysics, **61**, 1050–1064.

Griffiths, D., 2008, Introduction to electrodynamics: Prentice-Hall of India Private Limited New Delhi-110 001.

Grimm, R., 2009, Electromagnetic sounding of solid planets and satellites: Decadal Survey White Paper.

Grimm, R., E. Heggy, S. Clifford, C. Dinwiddie, R. McGinnis, and D. Farrell, 2006, Absorption and scattering in ground-penetrating radar: Analysis of the bishop tuff: Journal of Geophysical Research: Planets (1991–2012), **111**.

Grimm, R., D. Stillman, P. Sava, and D. Ittharat, 2014, Radio reflection imaging of asteroid and comet interiors II: Results and Recommendations: Adv. Space Res., submitted for publication.

Heggy, E., E. Asphaug, R. Carley, A. Safaeinili, and K. Righter, 2006, Dielectric properties of chondrites and their implication in radar sounding of asteroid interiors: LPI Contributions, **1325**, 45–46.

Henrique, A., W. Kofman, T. Hagfors, G. Caudal, and J.-P. Ayanides, 1999, A characterization of a comet nucleus interior: inversion of simulated radio frequency data: Planetary and Space Science, **47**, 885–904.

Hilton, J., 2002, Asteroid masses and densities: Asteroids III, University of Arizona Press.

Huebner, W., and J. Greenberg, 2001, Methods for determining material strengths and bulk properties of NEOs: Adv. Space Res., **28**, 1129–1137.

Johansson, M. E., and E. J. Mast, 1994, Three-dimensional ground-penetrating radar imaging using synthetic aperture time-domain focusing: SPIE's 1994 International Symposium on Optics, Imaging, and Instrumentation, International Society for Optics and Photonics, 205–214.

Kofman, W., A. Herique, J.-P. Goutail, T. Hagfors, I. P. Williams, E. Nielsen, J.-P. Barriot, Y. Barbin, C. Elachi, P. Edenhofer, A.-C. Levasseur-Regourd, D. Plettemeier, G. Picardi, R. Seu, and V. Svedhem, 2007, The Comet Nucleus Sounding Experiment by Radiowave Transmission (CONSERT): A Short Description of the Instrument and of the Commissioning Stages: Space Sci. Rev., **128**, 413–432.

Kruk, J. v. d., C. Wapenaar, J. Fokkema, and P. Van den Berg, 2003, Three-dimensional imaging of multicomponent ground-penetrating radar data: Geophysics, **68**, 1241–1254.

Leinhardt, M., C. D. Richardson, and T. Quinn, 2000, Body simulations of rubble pile collisions: Icarus, **146**, 133–151.

Lopez-Sanchez, M. J., and J. Fortuny-Guasch, 2000, 3-d radar imaging using range migration techniques: Antennas and Propagation, IEEE Transactions on, **48**, 728–737.

Lorrain, P., and D. Corson, 1962, Introduction to electromagnetic fields and waves: Freeman.

Michel, P., W. Benz, and C. D. Richardson, 2004, Catastrophic disruption of asteroids and family formation: a review of numerical simulations including both fragmentation and gravitational reaccumulations: Planetary and Space Science, **52**, 1109–1117.

Miller, R. D., J. H. Bradford, K. Holliger, and R. B. Latimer, 2010, Advances in near-surface seismology and ground-penetrating radar: SEG Books.

Moran, L. M., J. R. Greenfield, A. S. Arcone, and J. A. Delaney, 2000, Multidimensional gpr array processing using kirchhoff migration: Journal of Applied Geophysics, **43**, 281–295.

Nolan, C. M., C. Magri, S. E. Howell, M. L. Benner, D. J. Giorgini, W. C. Hergenrother, R. S. Hudson, S. D. Lauretta, J.-L. Margot, J. S. Ostro, and J. D. Scheeres, 2013, Shape model and surface properties of the OSIRIS-REx target asteroid (101955) bennu from radar and lightcurve observations: Icarus, **226**, 629–640.

Olhoeft, G., and D. Strangway, 1975, Dielectric properties of the first 100 meters of the moon: Earth and Planetary Science Letters, **24**, 394–404.

Picardi, G., D. Biccari, R. Seu, J. Plaut, W. Johnson, R. Jordan, A. Safaeinili, D. Gurnett, R. Huff, R. Orosei, O. Bombaci, D. Calabrese, and E. Zampolini, 2004, MARSIS: Mars Advanced Radar for Subsurface and Ionosphere Sounding: Mars Express - The Scientific Payload, **ESA SP-1240**, 51–69.

Plessix, R., 2006, A review of the adjoint-state method for computing the gradient of a functional with geophysical applications: Geophysical Journal International, **167**, 495–503.

Pratt, G., and Worthington, 1990, Inverse theory applied to multi-source cross-hole tomography. part 1: acoustic wave-equation method: Geophysical Prospecting, **38**, 287–310.

Pravec, P., W. A. Harris, and Michalowski, 2002, Asteroid rotations: Asteroids III, **113**, 113–123.

Prussing, E. J., A. B. Conway, and E. J. Prussing, 1993, Orbital mechanics: Oxford University Press New York, **57**.

Reynolds, J. M., 2011, An introduction to applied and environmental geophysics: John Wiley & Sons.

Richardson, D., Z. Leinhardt, H. Melosh, W. Bottke, and E. Asphaug, 2002, Gravitational aggregates: evidence and evolution: Asteroids III, University of Arizona Press.

Safaeinili, A., E. Asphaug, M. Belton, K. Klaasen, S. Ostro, J. Plaut, and D. Yeomans, 2005, Deep Interior Mission: Imaging the interior of near-Earth Asteroids using radio reflection tomography: Workshop Radar Investig., Lunar Planet Inst., Houston, TX, Expanded Abstracts, 6017.

Safaeinili, A., S. Gulkis, M. Hofstadter, and R. Jordsn, 2002, Probing the interior of asteroids and comets using radio reflection tomography: Meteor. & Planet. Sci., **37**, 1953–1963.

Sava, P., D. Ittharat, R. Grimm, and D. Stillman, 2014, Radio reflection imaging of asteroid and comet interiors I: Acquisition and Imaging Theory: Adv. Space Res., submitted for publication.

Sena, R. A., L. P. Stoffa, K. M. Sen, et al., 2003, Split step fourier migration of ground penetrating radar data: 73rd Annual International Meeting, Society of Exploration Geophysicists, Expanded Abstracts, 1023–1026.

Seu, R., R. Phillips, D. Biccari, R. Orosei, A. Masdea, G. Picardi, A. Safaeinili, B. Campbell, J. Plaut, L. Marinangeli, S. Smrekar, and D. Nunes, 2007, SHARAD sounding radar on the Mars Reconnaissance Orbiter: Journal of Geophysical Research, **112**, E05S05.

Stillman, D., and R. Grimm, 2011, Radar penetrates only the youngest geological units on mars: Journal of Geophysical Research: Planets, **116**, E03001.

Tanga, P., A. Cellino, P. Michel, V. Zappalà, P. Paolicchi, and A. Dell'Oro, 1999, On the size distribution of asteroid families: The role of geometry: Icarus, **141**, 65–78.

Tarantola, A., 1984, Inversion of seismic reflection data in the acoustic approximation: Geophysics, **49**, 1259–1266.

Walker, J., E. Sagebiel, and W. Huebner, 2006, A preliminary analysis of seismological techniques to study Eros and other asteroids: Adv. Space Res., **37**, 142–152.

Weissman, P., E. Asphaug, and S. Lowry, 2004, Structure and density of cometary nuclei: Comets II, University of Arizona Press.